Remote Sensing of Environment
December 2016, Volume 187 Pages 169-185
http://dx.doi.org/10.1016/j.rse.2016.10.015
http://archimer.ifremer.fr/doc/00355/46574/

Rain footprints on C-band synthetic aperture radar images of the ocean - Revisited

Alpers Werner [1, *], Zhang Biao [2, 3], Mouche Alexis [4], Zeng Kan [5], Chan Pak Wai [6]

[1] Institute of Oceanography, University of Hamburg, Bundesstrasse 53, 20146 Hamburg, Germany
[2] School of Marine Sciences, Nanjing University of Information Science and Technology, 219 Ningliu Road, Nanjing 210044, China
[3] Jiangsu Research Center for Ocean Survey and Technology, Nanjing, China
[4] Laboratoire d'Océanographie Spatiale, IFREMER, 29280 Plouzané, France
[5] Ocean Remote Sensing Institute, Ocean University of China, 5 Yushan Road, Qingdao 266003, China
[6] Hong Kong Observatory, 134A Nathan Road, Tsim Sha Tsui, Hong Kong

* Corresponding author : Wermer Alpers, email address : alpers@ifm.uni-hamburg.de

Abstract :

It is well known that rain leaves footprints on the sea surface that sometimes become visible on synthetic aperture radar (SAR) images. Rain cells can easily be detected on SAR images at all radar frequencies when they are associated with a downdraft pattern. But rain cells are not always associated with downdraft and rain can also occur in other forms, as stratified rain, rain bands, and squall lines. It turns out that radar signatures of rain at C-band are much more complex than at L- or X-band radar and that it is particularly difficult to identify unambiguously rain events on C-band SAR images acquired over the ocean. This is because C-band lies in the transition region where raindrops impinging onto the sea surface can increase (usually) or decrease the backscattered radar power and where volume scattering and attenuation by rain drops in the atmosphere are not always negligible (at very high rain rates). In order to get an insight into the physical mechanisms causing the C-band radar signatures of rain, we first revisit results obtained from historic laboratory and field experiments and multi-frequency/multi-polarization SAR data acquired during the SIR-C/X-SAR spaceshuttle mission in 1994. Then we analyze several C-band SAR images acquired by the European satellites Envisat and Sentinel-1A, and the Canadian satellite Radarsat-2 and compare them, whenever possible, with quasi-coincident and collocated weather radar images. The observational data show that, at low to medium rain rates, the main physical mechanism causing C-band radar signatures of rain is Bragg scattering at ring waves generated by the rain drops impinging onto the sea surface, which increase the radar backscatter. However, areas of increased radar backscatter are often accompanied by adjacent areas of decreased radar backscatter, which is due to attenuation of the Bragg waves by turbulence also generated by the impinging rain drops. Furthermore, we present a full-polarimetric Radarsat-2 SAR image of a rain cell together with a polarimetric decomposition analysis, which shows that the C-band radar signature of a rain cell is caused by surface scattering. The observation show that radar signatures of rain cells often contain segments, where the co-polarized as well the cross-polarized radar backscatter are strongly enhanced, which indicates non-Bragg scattering contributions to the scattering process. Furthermore, the polarimetric decomposition analysis shows that the C-band radar signature of a rain cell is dominated by surface scattering. Possible mechanisms, like scattering at splash products, are discussed. Whether the normalized radar cross section (NRCS) due to rain is increased or decreased depends on rain rate, wind speed, incidence angle, and history of the rain event. At low to moderate wind speeds (< 10 ms− 1) and low to medium high rain rates (< 50 mm h− 1), the NRCS is usually increased by up to 8 dB, and at high wind speeds (> 10 m s− 1) and low to high rain rates (but < 50 mm h− 1), the NRCS is usually decreased by up to 3 dB.

Highlights

► C-band radar signatures of a rain over the ocean are caused by surface scattering. ► At C-band, rain over the ocean can increase or decrease the radar backscatter. ► Scattering at ring waves is the dominant scattering mechanism at C-band. ► Rain can cause strong increase in co-polarized and cross-polarized backscatter. ► Non-Bragg scattering often contributes to the radar backscatter at C-band.

Keywords : Rain over the ocean, Synthetic aperture radar, Sea surface winds, C-band radar backscattering, Ring waves

1. Introduction

Since synthetic aperture radar (SAR) images from the American Seasat satellite became available in 1978 it is known that SAR images acquired over the ocean often capture radar signatures of rain (Fu & Holt, 1982). The early studies have concentrated on radar signatures of tropical rain cells, where the downdraft (or downburst) of cold air is the principal contributor to the radar signature (Atlas, 1994). However, downdraft occurs only in a certain stage of the life cycle of a rain cell (in the dissipating stage where it is associated with light rain), while in the mature stage, associated with heavy rain, updraft and downdraft are co-existing. Verification that some features visible on SAR images are caused by convective rain, like rain cells, squall lines, and supercells, has been provided by quasi-simultaneously acquired weather radar data (Lin et al., 2001; Melsheimer et al., 2001). While convective rain is the dominant type of rain in the tropics and subtropics (50 to 80 %), stratiform rain dominates in the high latitudes, but remains poorly studied. Both kinds of rain affect the radar backscatter from the sea surface.

Rain over the sea is a main source of error in the retrieval of near-sea surface winds from scatterometer data. The effect of rain on radar backscatter has been studied extensively for Ku-band (14 GHz) scatterometers, like the ones flown on the American Quikscat satellite and the Indian Oceansat 2 satellite (Contreras et al., 2003; Weissman et al., 2005; Weissman & Bourassa 2008, 2011), and recently also for C-band (5.3 GHz) scatterometers, like the Advanced Scatterometer (ASCAT) onboard the European MetOp satellites (Portabella et al., 2012; Lin et al., 2013, 2014, 2015). In particular, the effect of rain on C-band radar backscattering over the ocean using satellite data has been investigated so far only by applying statistical methods. Lin et al. (2013) correlated wind data retrieved from ASCAT data with wind data calculated from an atmospheric model and with rain data retrieved from the Tropical Rainfall Measuring

Mission (TRMM). Xu et al. (2015) also used a statistical method to demonstrate the influence of rain on C-band radar backscatter by using Envisat SAR data, wind data from a weather forecast model, and rain rate data from a weather radar. In contrast to these studies, in this paper we investigate signatures of individual rain events with the aim to identify the physical mechanisms causing the observed C-band radar signatures of rain over the ocean.

However, the foremost motivation for this study is to improve the identification of radar signatures of rain events on C-band SAR images acquired over the ocean. It is often difficult to determine unambiguously whether a radar signature visible on a SAR image of the sea surface results from rain or another phenomenon. C-band radar signatures of rain are particular complex because they can consist of areas of increased or decreased radar backscatter relative to the background depending on rain rate, wind speed, incidence angle, and the time evolution of the rain event. The study of radar signatures of rain cells is a difficult task since concurrent data for validation are seldom available. However, we found in the archives of the European Space Agency (ESA) and the Canadian Space Agency (CSA) several C- band SAR images acquired over the ocean showing radar signatures of rain cells for which concurrent weather radar are available. Studies using high-resolution SAR data are also complementary to scatterometer studies for discriminating between the different physical mechanisms causing the variations of the radar backscatter at scatterometer-scale resolution (typically tens of kilometers).

In order to get an insight into the physical mechanisms causing C-band radar signatures of rain, it is quite helpful to analyze SAR images of rain cells acquired simultaneously at different radar frequencies and polarizations. To this end, we have revisited data that were acquired by 1) by a multi-frequency (S-, C-, X-band) and multi-polarization (HH, VV, HV) coherent scatterometer mounted on a tower located at the shore of the North Sea (Braun, 2002; Braun & Gade, 2006) and 2) a multi-frequency (L-, C-, and X-band) multi-polarization (VV, HH, VH, HV) SAR flown on the spaceshuttle Endeavour in 1994 during the Spaceborne Imaging Radar-C/X-band SAR (SIR-C/X-SAR) mission (Jordan et al., 1995; Jameson et al. 1997; Melsheimer et al., 1998; Alpers & Melsheimer, 2004). Here X, C, S, and L denote radar bands in the frequency (wavelength) ranges 7.5-12 GHz (2.5- 4 cm), 3.75-7.5 GHz (4-8 cm), 2-3.75 GHz (5-8 cm), and 1-2 GHz (15-30 cm), respectively, and VV, HH, VH, HV denote the polarization combination at which the radar signals are emitted and received, e.g., VH denotes that the signal is emitted at vertical polarization and received at horizontal polarization.

The paper is organized as follows: In Section 2 we review the physical mechanisms causing the radar signatures of rain. In Section 3 we present several SAR images of rain events acquired by (1) the L-band SAR on the American satellite Seasat, (2) the multi-frequency/multi - polarization SAR from the SIR-C/X-SAR spaceshuttle mission, (3) the C-band SAR on the European Sentinel-1A satellite, (4) the fully polarimetric C-band SAR on the Canadian Radarsat-2 satellite, and (4) the C-band SAR on the European Envisat, termed Advanced SAR (ASAR). For the Radarsat-2 SAR image and for all five Envisat SAR images presented in this paper we have concurrent weather radar images available for validation. In Section 4 we discuss how these results relate to studies on the rain effects on the retrieval of ocean surface winds from C-band scatterometer data. In Section 5 we discuss the results presented in the previous sections, and in Section 6 we summarize them. In the Appendix we recall some basics of polarimetric decompostion that is needed for interpreting the quad-polarization Radarsat-2 image presented in Section 3.4.

2. Scattering mechanisms

In many papers dealing with radar signatures of rain over the ocean it is assumed that four physical processes contribute to the radar signature (for a review, see, e.g., Alpers & Melsheimer, 2004; Xu et al., 2015): 1) scattering of the radar pulse at the sea surface whose roughness is modified by ring wave generation and wave damping due to turbulence caused by rain drops impinging onto the sea surface, 2) increase of the sea surface roughness due to downdraft winds often associated with rain cells, 3) scattering at splash products, i.e., at craters, stalks, crowns, and rain drops bouncing upwards, which are also generated by the impinging rain drops, and 4) scattering and attenuation of the radar pulse by raindrops (hydrometeors) in the atmosphere (volume scattering and attenuation).

2.1. Surface scattering

Usually radar backscattering from the sea surface at incidence angles between $25^o \leq \theta \leq 70^o$ and at low to moderate wind speeds (< 8 m s^{-1}) is described by Bragg scattering theory (Valenzuela, 1978; Robinson, 2004). However, it has been realized that, in addition to Bragg scattering, also incoherent scattering from surface disturbances associated with by breaking waves contributes to the backscattering (Zavorotny & Voronovich, 2001; Kudryavtsev et al., 2003; Mouche et al., 2007). This contribution is considered to be important for explaining HH and cross-polarized observations.

According to Bragg scattering theory the normalized radar cross section (NRCS) is proportional to the spectral energy density at the Bragg wavelength (λ_B), which is related to the radar wavelength (λ_0) and the incidence angle (θ) by

$$\lambda_B = \lambda_0 / 2 \sin \theta \qquad (1)$$

*R*ain drops impinging onto the water surface generate ring waves which scatter the incident radar pulse. For C-band SARs with a wavelength of λ_0=5.3 cm (like the ones on ERS-1, ERS-2, Envisat, Radarsat-2, and Sentinel-1A), the water waves responsible for the radar backscattering (the Bragg waves) have wavelengths in the range 3.0 cm $\leq \lambda_B \leq$ 6.7 cm (assuming $25^o \leq \theta \leq 70^o$). This wavelength range can be converted into a frequency range by using the dispersion relation for gravity-capillary waves

$$f=1/2\pi \, (gk+\gamma k^3/\rho)^{1/2} \qquad (2)$$

where f is the frequency, g the gravitational constant (9.81 m s^{-1}), $k=2\pi/\lambda$, γ the surface tension for water (0.074 N m^{-1}), and ρ the density of water (1000 kg m^{-3}). Inserting in Eq. (1) the values λ=3.0 cm and λ=6.7 cm, we obtain f=5.0 Hz and f=8.3 Hz, respectively. Thus only those gravity-capillary waves having frequencies in the range 5.0 Hz $\leq f \leq$ 8.3 Hz can serve as Bragg waves in C-band radar backscattering. As will be discussed later, scattering mechanisms other than Bragg scattering may also contribute to surface scattering.

2.1.1. Laboratory measurements

Ring wave generation by artificial rain has been studied extensively in the laboratory in the 1990's and early 2000's at NASA's Wallops Flight Facility (Bliven et al., 1993, 1997) and the University of Hamburg (Braun, 2002; Braun et al., 2002; Braun & Gade, 2006). Bliven et al. (1997) carried out experiments at the Rain-Sea Interaction Facility at Wallops, where they released droplets of 2.8 mm diameter from a height of 17 m such that the speed of the droplets when impacting onto the water surface was close to the theoretical terminal velocity of 7.8 m s^{-1}. In Fig. 1 the spectral energy density of the ring waves as measured by Bliven et al. (1997) is depicted. It shows that the water surface gets rougher, i.e., the spectral energy density increases, when the rain rate increases, while the spectral shape remains very stable. The peak of the ring wave spectrum is located at 5.68 +/- 0.12 Hz. The frequency spectra can be converted into wavenumber spectra by using the dispersion relation for gravity-capillary waves (see Eq. (1)). It turns out that the spectral peak in the wavenumber domain is located at 1.18 rad cm^{-1} corresponding to 5.3 cm. (Bliven et al., 1997), which lies well in the wavelength range of the C-band Bragg waves (3.0 cm $\leq \lambda_B \leq$ 6.7 cm). The frequency range of the C-band Bragg waves (5.0 Hz $\leq f \leq$ 8.3 Hz) is marked by a thick horizontal line in Fig. 2. However, ring wave spectra generated by rain over the ocean depend also on the drop size distribution (Marshall & Palmer, 1948), which varies with rain type (Lemaire et al., 2002).

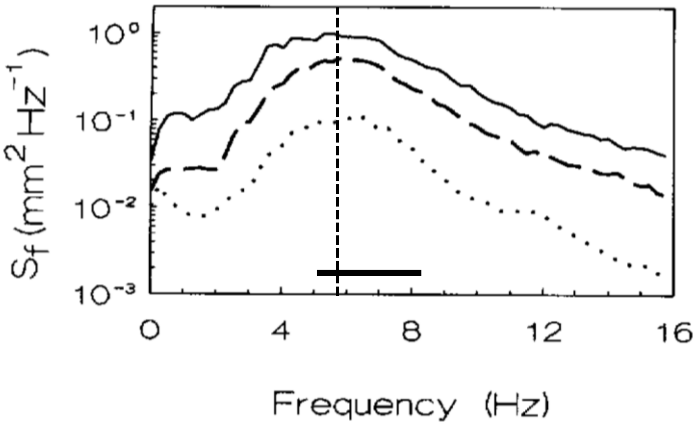

Fig. 1. Ring wave frequency spectrum as measured in the laboratory for rain rates of 5 (dotted line), 50 (dashed line), and 200 mm h^{-1} (solid line). The peak of all three spectra is located around 5.7 Hz. corresponding a wavelength of 5.3 cm. The inserted thick horizontal line at the bottom marks the frequency range of those ring waves which serve as Bragg waves in C-band radar backscattering. Reproduced from Bliven et al. (1997).

Laboratory measurements with artificial rain employing a Ku-band (13.5 GHz) and a Ka-band (36 GHz) scatterometer (VV polarization, 30^{o} incidence angle) and an ultra-high speed digital camera synchronized with the radar data acquisition were carried out also at the Rain-Sea Interaction Facility at Wallops (Sobiesky & Bliven, 1995). These measurements show that ring waves are the dominant contributors to the radar backscattering and that scattering at stalks is much smaller, but not negligible. Their Ku-band data show further that the crowns contribute 3.7%, the craters and stalks 19.1%, and the ring waves 75.2 % to the radar backscattering. Although all these laboratory measurements were carried out with scatterometers operating at higher radar frequencies than C-band, we expect that radar backscattering at splash products should also contribute to the radar backscattering at C-band.

2.1.2. Field measurements

Radar backscattering measurements with a multi-frequency/multi-polarization scatterometer operating at S-band (2.4 GHz), C-band (5.3 GHz), and X-band (10 GHz) and at VV, HV, and HH polarizations were carried out by the University of Hamburg from a shore-based tower located at the mouth of the river Elbe in the German Bight of the North Sea (Braun & Gade, 2006). The Doppler spectra (not reproduced here) show that Bragg scattering at ring waves is the dominant scattering mechanism causing the enhancement of the C-band co-polarized radar backscatter in the presence of rain. However, these measurements also show that at cross-polarization the C-band Doppler spectrum has a strong maximum at zero Doppler frequency, i.e., at a frequency that is not related to the phase velocity of ring waves (Fig. 6(b) in their paper). This suggests that another scattering mechanism other than Bragg scattering must contribute to the C-band radar backscattering backscatter in the presence of rain. This could be scattering at splash products consisting of craters, crowns, stalks, and rain drops bouncing upwards, which are generated by rain drops splashing onto the sea surface.

The results of these measurements are depicted in Fig. 2. It shows the is the ratio of the NRCS at VV polarization in the presence of rain and the NRCS at VV polarization in the absence of rain ($\sigma^{o}_{vv,\ rain}/\sigma^{0}_{vv}$) as a function of Bragg wave number. Note that measurements at different Bragg wave numbers can be achieved at a fixed radar band by varying the incidence angle, see Eq. (1). Fig. 2 shows that at S-band (2.4 GHz) rain reduces the NRCS, at C-band (5.3 GHz) it sometimes reduces and sometimes enhances it, and at X-band (10.0 GHz) it always enhances it. In this plot all measurements have been lumped together for different rain rates (up to 12 mm h^{-1}) and wind speeds (between 4.5 and 17 m s^{-1}). However, the data show a clear trend: the higher the wave number, i.e., the higher the incidence angle (see Eq. (1)), the higher is the ratio $\sigma^{0}_{vv,\ rain}/\sigma^{0}_{vv}$, i.e., the higher is the increase in Bragg wave amplitude. Furthermore, they show that C-band lies in the transition region between reduction and enhancement of the NRCS due to rain. However, the data set was too sparse for obtaining reliable quantitative information on the dependence of the ratio on rain rate and wind speed. The wavenumber at which the fitted curve changes sign is located near 100 rad m^{-1}, corresponding to a Bragg wavelength of 6.3 cm, which lies in the lower end of the C-band Bragg wavenumber range (or the upper end of the C-band Bragg wavelength range: 3.0 cm $\leq \lambda_B \leq$ 6.7 cm).

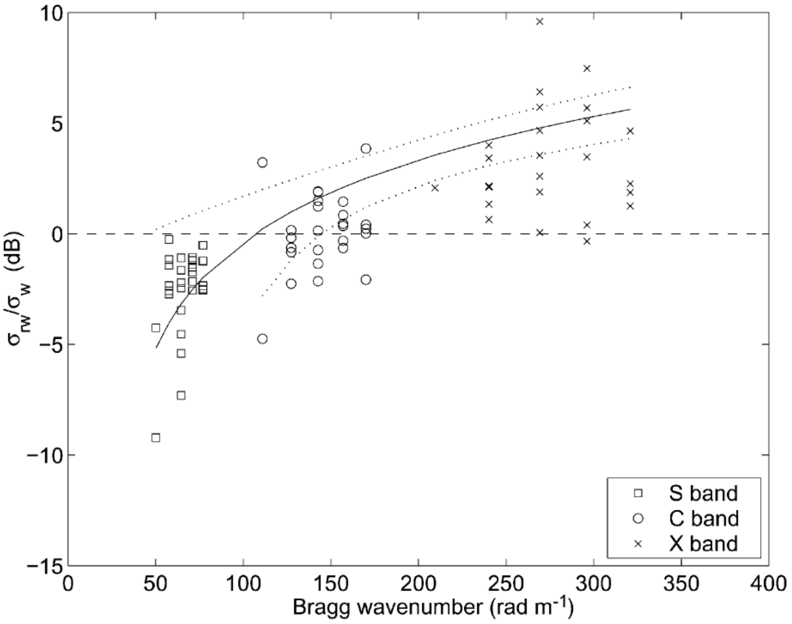

Fig. 2. Variation of the NRCS of ocean areas struck by rain as a function of Bragg wavenumber as inferred from data acquired by S-, C-, and X-band, multi-polarization scatterometers mounted on a shore-based tower. Plotted is the ratio of the NRCS at VV polarization in the presence of rain and in the absence of rain as a function of the Bragg wavenumber. The solid line denotes a linear regression to the data, and the dotted lines denote the limits of the 95% confidence interval of this regression. Reproduced from Braun & Gade (2006).

2.2. Volume scattering and attenuation

At C-band, the attenuation and scattering of microwaves by raindrops in the atmosphere is very small for low to moderate rain rates at all polarizations and can be neglected. Only when the rain rate is larger than about 50 mm h^{-1} is the attenuation larger than 1 dB (Lin et al., 2001; Melsheimer et al., 2001). Lin et al. (2001) have analyzed a C-band SAR image acquired by the ERS-2 satellite over the coastal waters south of Singapore which shows radar signatures of a strong tropical squall line. They concluded from the analysis of this SAR image together with weather radar images that attenuation of the radar pulse by rain drops in the atmosphere is the dominant mechanism in heavy rain areas (rain cores) with rain rates above 125 mm h^{-1}.

Volume scattering and attenuation by rain drops (or, more precisely, by hydrometeors which denote rain drops in the liquid as well as in the melting phase) have also been observed on C-band SAR images acquired over the South American rain forest, see Fig. 3. The Envisat ASAR image depicted in Fig. 3(a) shows a C-band SAR image which resembles very much X-band SAR images of rain cells acquired over the tropical rain forests (see Fig. 1 in Melsheimer et al. (1998) and Fig. 4 in Danklmayer et al. (2009)). The radar signature consists of a bright area and an adjacent dark area in the direction pointing away from the SAR antenna. The black arrows inserted in Fig. 3 denote the antenna look direction. We interpret the bright area as being caused by reflections from raindrops in the atmosphere (volume scattering), whereas the adjacent dark area (shadow) as being caused by rain-attenuated (blocked) radar signals from the ground. A sketch of the scattering geometry explaining this form of the radar signature can be found in Danklmayer et al. (2009), Fig. 9. Such forms of radar signatures of rain cells are less frequently observed at C-band than at X-band. But when they are observed, they are much weaker as evidenced by multi-frequency SAR images acquired over tropical rain forests during the SIR-C/X-SAR mission (Melsheimer, 1998). We suppose that such radar signatures are associated with very strong rain rates encountered frequently over tropical rain forest.

However, on C-band SAR images acquired over tropical rain forests, the radar signatures of rain cells are often not accompanied by adjacent dark areas (shadows). An example is shown in Fig. 3(b). Although we have no evidence from weather radars or other sensors, we interpret these bright features also as radar signatures of rain, but in this case associated with a melting layer. Melting layers, which cause very strong reflections, are often encountered in tropical and subtropical regions at heights of typical 4-6 km. When a radar pulse from a spaceborne SAR hits this layer, it is almost completely reflected and cannot penetrate into the lower layers where it would be attenuated by the rain drops. Thus, in this case, the bright patches caused by reflection are not followed by dark areas in look direction of the antenna. For more information on melting layers the reader is referred to the website http://www.radar.mcgill.ca/science/ex-phenomenon/ex-melting-layers.html.

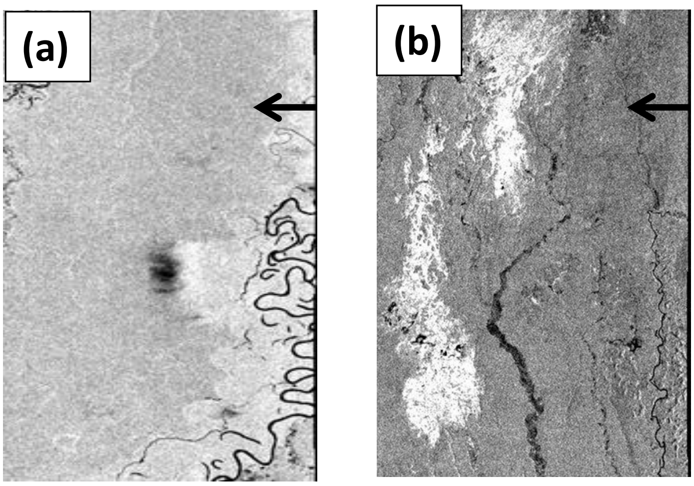

Fig. 3. (a) C-band SAR image acquired by the Advanced SAR (ASAR) onboard the Envisat satellite at VV polarization in the Image Mode (IM) (100 km swath width) during a descending satellite passes over the South American rain forest (a) on 24 April 2010 at 13:51 UTC and (b) on 10 February 2010 at 13:43 UTC. The inset black arrows denote the look direction of the SAR antenna. Note that in image (a) the bright patch is followed to the left by an adjacent dark patch caused by shadowing, while in image (b) no adjacent dark patches (shadows) are visible.

However, since we have no concurrent measurements from other sensors, our explanation of the origin of the C-band radar signature presented in Fig. 3(b) remains speculative. Although we favor the melting layer hypothesis, we cannot exclude that the radar signature in Fig. 3(b) may result from rain drops splashing onto the leaves of the trees in the dense rain forest.

3. Spaceborne SAR images

3.1. Seasat SAR image

As mentioned before, convective rain in the form of rain cells is often associated with a downdraft which increases the sea surface roughness (Fig. 4(a)). Rain cells have diameters of typically 5 to 20 km and appear often in clusters. When there is no ambient wind, the downdraft becomes visible on a SAR image of the sea surface as a quasi-circular pattern, but when there is an ambient wind, the pattern is distorted and becomes elliptical. Fig. 4(b) shows such a downdraft pattern on a Seasat SAR image acquired over the Gulf of Mexico (Fu & Holt, 1982). The SAR onboard the American Seasat satellite (launched 1978) operated at a radar wavelength of 23.5 cm (L-band). In contrast to radar signatures of rain caused by the mechanisms discussed in Section 2, the radar signature of a downdraft pattern depends very little on radar frequency. Although this paper deals with C-band radar signatures of rain cells, we present this L-band Seasat SAR image here because it shows an important feature that is also seen frequently on C-band SAR images of rain cells: the bright patch in the dark area in the center of the downdraft pattern. We interpret the bright patch as being caused by scattering at splash products generated by impinging rain drops onto the sea surface (Atlas, 1994). It can be excluded that the bright patch in the L-band Seasat radar image results from scattering at rain drops in the atmosphere, because volume scattering is very small at a radar wavelength of 23.5 cm and can be neglected, even at very high rain rates.

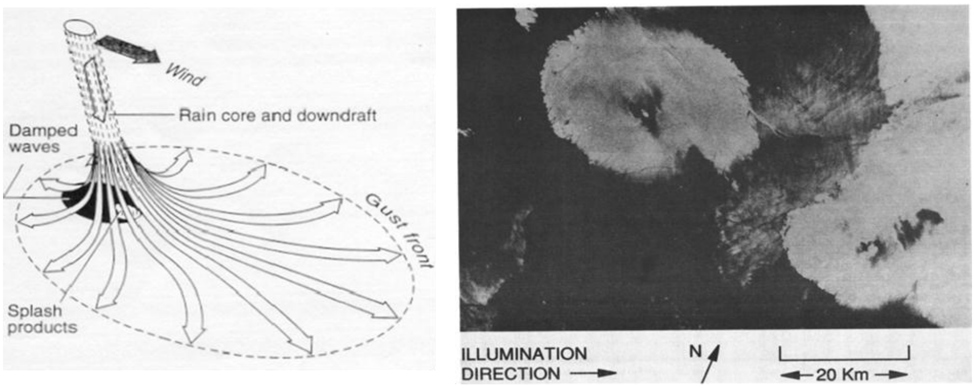

(a) (b)

Fig. 4. (a) Schematic sketch of the downdraft of a rain cell spreading over the sea surface where it causes roughening of the sea surface (adapted from Atlas, 1994); (b) Seasat SAR image acquired over the Gulf of Mexico on 11 September 1978 at 17:14 UTC showing at the upper left an elliptically-shaped bright downdraft pattern with a black area in the center, which contains a small bright patch. Adapted from Fu & Holt (1982).

3.2. *SIR-C/X-SAR images*

Multi-frequency, multi-polarization SIR-C/X-SAR images are of great value for getting further insight into the physical mechanisms causing the C-band radar signatures of rain. An example of a strong rain cell imaged by SIRC/X-SAR is depicted in Fig. 5. It shows that the radar signature depends strongly on radar frequency. At L-band, the radar signature consists at all polarizations of a dark patch (often surrounded by a bright area caused by downdraft), while at C-band, it consists of a bright patch, which is located in the same area as the dark patch in the L-band images. Since in the C-band image no dark patch is visible on the rightft hand side of the bright patch, i.e., on the side furthest away from the SAR antenna (like in Fig. 3(a)), and since the dark and bright areas are located at the same position in the L-band image and the C-band image, respectively, we conclude that the bright patch in the C-band image must be caused by surface

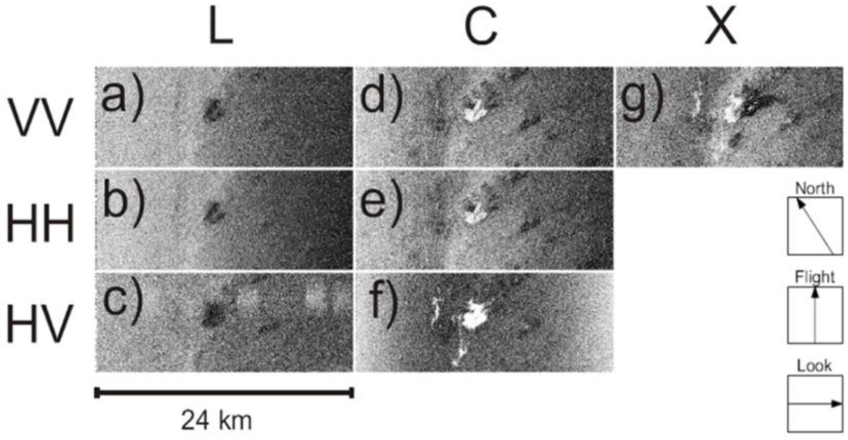

Fig. 5. Multi-frequency, multi-polarization SIR-C/X-SAR images acquired simultaneously at L-, C-, and X-band over the Gulf of Mexico on 18 April 1994 at 08:11 UTC showing the strong dependence of the radar signature on radar frequency and polarization. Reproduced from Melsheimer (1998).

scattering. The dark patches in the L-band image are caused by damping of L-band Bragg waves, which have wavelengths around 25 cm, by turbulence generated by the rain drops impinging onto the sea surface, while the bright patches in the C-band image are caused by those ring waves generated the impinging rain drops that match the Bragg resonance condition (see Eq. (1)) and which have wavelengths around 5 cm. A quantitative analysis of the variation of the NRCS along a transects through the rain cells has yielded the following results (Melsheimer, 1998): At L-band, VV polarization, the decrease of the NRCS relative to the background is around 5 dB in the rain cell area, and at C-band, VV polarization, the increase is around 2 dB. This is in agreement with the field measurements described in Subsection 2.1.2 and complies with the theory on the generation of radar signatures of rain cells presented there.

As discussed already in Subsection 2.1.2 and evidenced by Fig. 2, C-band radar signatures of rain cells lie in the transition region, where the impinging rain drops can cause a decrease or an increase of the NRCS depending on rain parameters, like rain rate and drop size distribution, as well as on wind speed. Since these parameters can be quite variable within a rain event, rain areas often manifest themselves in C-band SAR images of the sea surface as a mixture of bright and dark areas. This fact can be used to identify areas of stratified rain on C-band SAR images of the sea surface, see Figs. 13(a), 14(a), and 16(a). Large mean standard deviations of the NRCS are indicative for rain areas. Note that in the C-band HH- and VV-polarization images depicted in Fig. 5 also a small area with decreased NRCS value is visible in the center of the downdraft pattern. This dark area is not located behind the bright area in look direction of the antenna, which would be an indication of attenuation of the radar beam by rain drops in the atmosphere (shadowing). But dark areas adjacent to bright areas located on the side furthest away from the SAR antenna caused by attenuation of the radar beam by rain drops in the atmosphere are not expected to occur in C-band SAR images, except for very high rain rates (see Subsection 2.2). However, in X-band SAR images, such pattern are commonly observed. At this radar band, the radar signature of rain cells is primarily caused scattering and attenuation at rain drops in the atmosphere.

The most startling feature in this set of SAR images is the large increase of the NRCS in the C-band cross-polarization (HV) image in the rain-struck area. NRCS scans along transects through this rain cell have yielded the following results (Braun, 2002): In the rain cell, the C-band NRCS at HH and VV polarizations increases by 2 dB and at cross-polarization it increases by 10 dB. Clearly, this strong increase at cross-polarization cannot be explained by Bragg scattering within a composite surface model (Romeiser et al., 1997). Thus another scattering mechanism must be responsible for such an increase. One possible mechanism is scattering by rain drops in the atmosphere, another one is scattering at splash product generated by the impinging rain drops onto the sea surface. As we shall see in Subsections 3.3 and 3.4, also Sentinel-1A and Radarsat-2 images show a similar large increase of the NRCS at cross-polarization (up to 8 dB) in the rain cell areas. It is very likely that this increase is caused by scattering at splash products and not by a poor performance of the SIR-C/X-band C-band SAR. In principle, it could be caused by a poor isolation between the co-polarized and the cross-polarized channels, termed "cross-talk", which is very unlikely. The C-band SARs on Radarsat-2 and Sentinel-1A are known to have a very good inter-channel calibration. E.g., for Radarsat-2, the inter-channel isolation is better than -45 dB (Vachon & Wolfe, 2011), which is much lower than the NRCS values reported in this paper.

3.3. *Sentinel-1A image*

Figs. 6(a) and 7(a) show two sub-scenes of a C-band SAR image that was acquired by the Sentinel-1A satellite during a descending satellite pass in the Interferometric Wide (IW) swath mode (swath width: 250 km, resolution: 5 m x 20 m) at VV and VH polarizations on 9 June 2015 at 21:53:41 UTC over the South China Sea east of the Philippine island of Luzon. They show radar signatures of several rain cells. The sub-scenes analyzed here were imaged at an incidence angle aound 40^{o}. While the VV images show the downdraft pattern of the rain cells, the VH images do not show them. This is due to the fact that the NRCS at crosspolarization is lower than the floor of the Sentinel-1A SAR. As will be shown in Section 3.4, this is different from Radarsat-2 images, where downdraft patterns are also visible in VH images, because Radarsat-2 SAR has a much lower noise floor (-32.dB) than of the Sentinel-1A SAR (-27.5 dB). Figs. 6(c) and 6(d) show the variations of the NRCS along the two transects inserted in Figs. 6(a) and 6(b), and Fig.

7(c) and Fig. 7(d) show the variations of the NRCS along the two transects inserted in Figs. 7(a) and 7(b). The speed of the ambient wind was around 2.5 m s^{-1}, i.e., around the threshold for short wave (ripple wave) generation. Note that the two downdraft patterns have quasi-circular shape caused by the very low ambient wind.

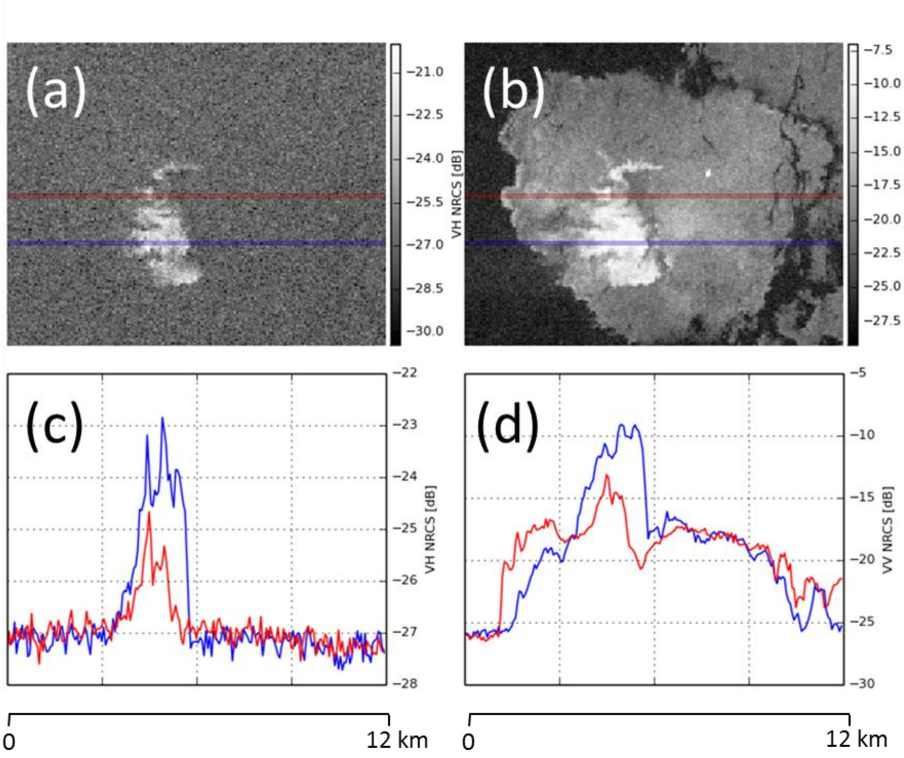

Fig. 6. (a), (b) Section of a Sentinel-1A SAR image acquired on 9 June 2015 at 21:53:41 UTC over the South China Sea, west of the Philippine island of Luzon, showing the radar signatures of a rain cell at VH (a) and VV (b) polarizations; (c), (d) NRCS scans along the two transects inserted in the images.

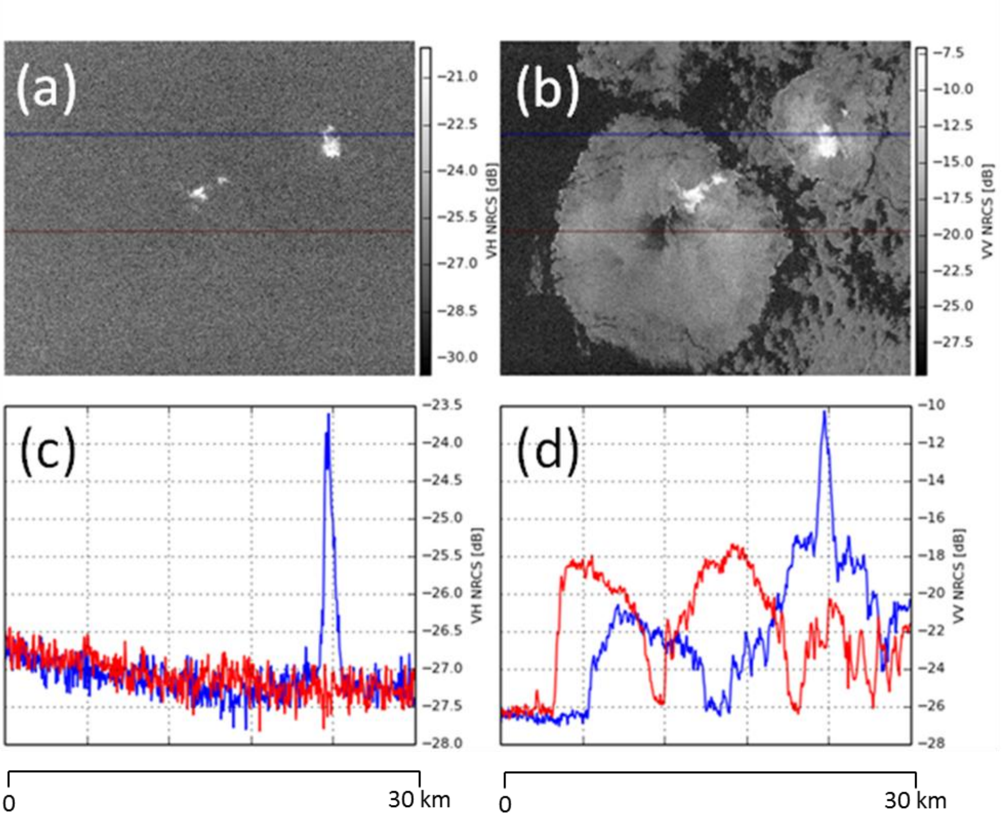

Fig. 7. (a), (b) Another section of the Sentinel-1A SAR acquired on 9 June 2015 at 21:53:41 UTC showing the radar signatures of two rain cells at VH (a) and VV (b) polarizations; (c), (d) NRCS scans along two transects inserted in the images.

Figs. 6(c) and 6(d) show along the lower (blue) transect an increase of the NRCS at VH polarization in the rain cell of 4 dB and at VV polarization an increase of 7 dB relative to the surrounding downdraft area. Figs. 7(c) and 7(d) show along the transect through the small rain cell in the upper right of the image an increase of the NRCS at VH polarization in the rain cell of 3.5 dB and at VV polarization an increase of 7 dB relative to the surrounding downdraft area. However, the increase of the NRCS at VH polarization by 4 and 3.5 dB must be considered as an underestimation because the lowest NRCS values are clearly lower than the NESZ of the Sentinel-1A SAR.

The NRCS plots along the lower (red) transect in Fig. 7(b) shows quite impressively the variation of the NRCS at VV polarization caused by downdraft. The NRCS variation is almost symmetric with respect to the dark area visible in Fig. 7(b), which is in the center of the downdraft, where the horizontal wind should (theoretically) be zero. The red curve in Fig. 7(d) exhibits two maxima with values of -18 dB. At VV polarization and at an incidence angle of 40^o, this NRCS value corresponds to a wind speed of 4.5 m s^{-1}. Note that the bright area in this rain cell is located outside the dark area, which is different from the Seasat image (Fig. 4(b)). We interpret the dark patch in the center of the downdraft pattern in the Sentinel-1A image depicted in Fig. 7(b) as being caused by low wind speed. In the Seasat image, it just happened that the bright radar signature resulting from scattering at splash products is located in the center of the downdraft pattern (otherwise it would not have been detectable). However, in general, the sea surface areas hit by rain do not coincide with the low wind speed area in rain cells (see, e.g., also Fig. 4 of Melsheimer et al., 2001).

3.4. Radarsat-2 image

A quad-polarization (fully polarimetric) SAR image of Radarsat-2 showing the radar signature of a rain cell for which also a concurrent weather radar image is available for validation is shown in Fig. 8. This image was acquired during an ascending satellite pass on 15 July 2010 at 23:27 UTC over the Atlantic Ocean off the coast of Florida (near Fort Lauderdale). Since this image was acquired in the quad-polarization mode, we also could carry out a polarimetric decompostion analysis. It has been claimed, see e.g., Cloud & Pottier (1996) and Lee & Pottier (2009), that it is possible to identify scattering mechanisms causing observed radar signatures by polarimetric analysis, see Appendix. In Sub-section 3.4.1, we first present a multi-polarization radiometric analysis and then in Sub-section 3.4.2 a polarimetric decomposition analysis.

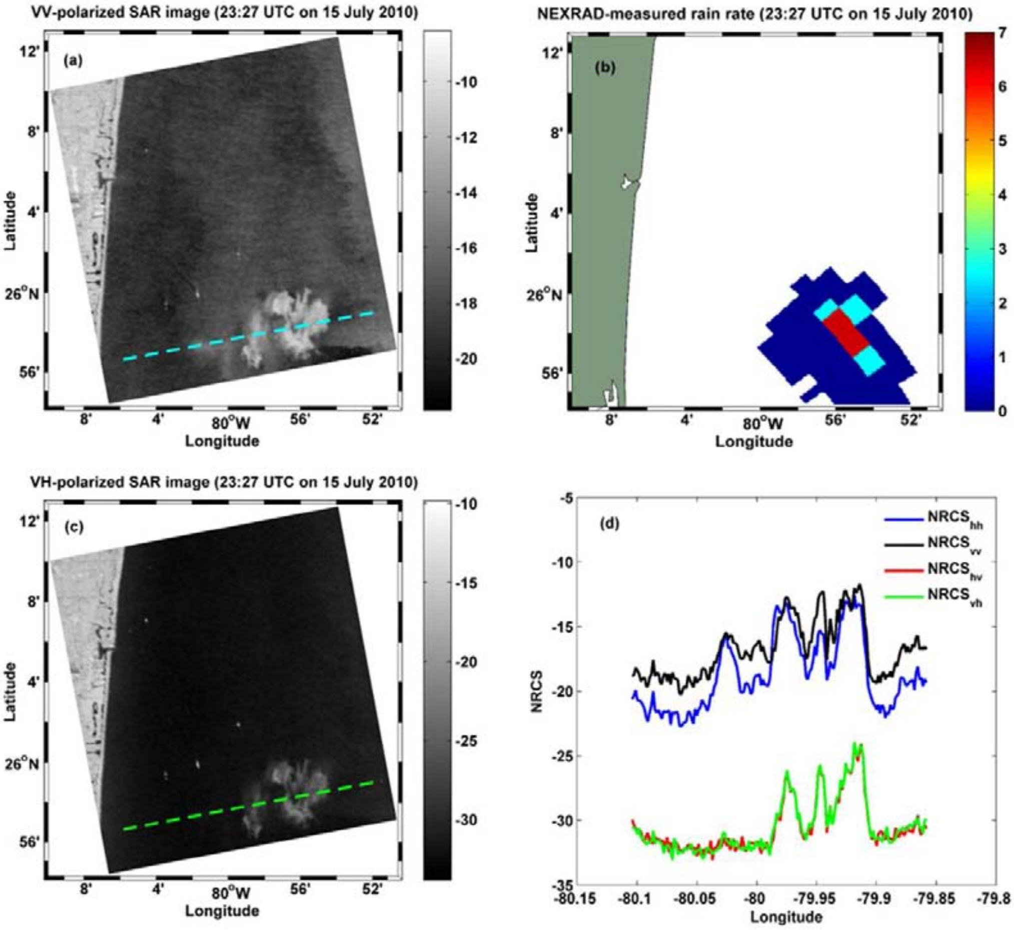

Fig. 8. C-band Radarsat-2 SAR image acquired in the quad-polarization mode on 15 July 2010 at 23:27 UTC off the coast of Florida (near Fort Lauderdale) showing the radar signature of a rain cell. (a) VV polarization image. (b) Next Generation Weather Radar (NEXRAD) Level III Precipitation Product (One-Hour Precipitation) on 15 July 2010 at 23:27 UTC. The rain rates varied in the rain cell between 1 and 7 mm h^{-1}. (c) VH polarization image. (d) Variation of the NRCS at HH (blue), VV (black), HV (red), and VH (green) polarizations along the transect inserted in the images.

3.4.1. Radiometric analysis

Figs. 8(a) and 8(c) show the C-band Radarsat-2 VV- and VH-polarized SAR images and Fig. 8(b) the Level III Preciptation Product (One-Hour Precipitation) acquired by the Next-Generation Radar（NEXRAD) on the same day at 23:27 UTC. NEXRAD is a network of high-resolution S-band Doppler weather radars operated by the National Weather Service (NWS) in the United States. The NEXRAD data show that rain rates varied in the rain cell between 1 and 7 mm h^{-1}. The variation of the NRCS at HH, VV, HV, and VH polarizations along the transect inserted in the images is depicted in Fig. 8(d). Radarsat-2 acquired this image at an incidence angle around 40^{o}. The NRCS plots in Fig. 8(d) show four pronouned peaks in the HH and VV curves, but only three pronounced peaks and one very small peak in the VH and HV curves. We attribute the very small peak in the HV and VH curves to the low signal-to-noise ratio in the cross-polarization channel. As shown by Vachon & Wolfe (2011), the instrument noise floor, i. e., NESZ, lies in the fine quad-polarization mode of Radarsat-2 for an incidence angle of 40^{o} between -33 and -34 dB (their Fig. 2), which is very close to the low value of cross-polarization NRCS in the rain-free area. However, in the co-polarized channels, the NRCS values are well above the noise floor, where the NRCS at VV polarization in the rain-free area is around -19 dB and at HH around -22 dB. At VV polarization, this value is consistent with composite surface Bragg scattering theory for a wind speed of 4 m s^{-1}. However, in the areas where the VV and HH NRCS curves have peaks due to the presence of rain, the VV and HH NRCSs are approximately equal (with the exception of the third peak) indicating non-ambiguous deviation from Bragg scattering. The NRCS at VV polarization varies in the rain area between 7 and 8.5 dB, at HH polarization between 2 and 7 dB, and at VH and HV polarizations between 6 and 8 dB.

The increase of the crosspolarization NRCS due to rain seems to be much higher (6-8 dB) in this Radarsat-2 image than in the two Sentinel-1A images depicted in Figs. 6 and 7 (3.5-4 dB). But this is an instrumental effect due to the large difference in the NESZ of both SARs, which is -32dB for Radarsat-2 SAR and -27.5 dB for Sentinel-1A SAR. Thus the Radarsat-2 data refelect best the strong increase of the crosspolarization NRCS due to scattering at splash products. The increase of the crosspolarization NRCS by 6-8 dB inferred from Radarsat-2 data is consistent with the increase by 10 dB inferred from C-band SIR-C/X data (see

Section 3.2). Differences in these NRCS values are probably due to differences in the rain rate and the background wind.

3. 4.2. Polarimetric decomposition analysis

SAR polarimetry has been applied quite successfully to classification of land targets (Cloud & Pottier, 1997; Lee & Pottier, 2009). It has also been applied to detection of oil floating on the sea surface (Migliaccio et al., 2007, 2009; Zhang et al., 2011; Skrunes et al., 2014), but its usefulness for this kind of application is still discussed controversially (Minchew et al., 2012). The reason is that sea areas covered with mineral oil or biogenic surface films have very low NRCS values, especially at cross-polarization. Therefore it is likely that some of the results obtained for this application are strongly affected by instrument noise as pointed out by Minchew et al. (2012). However, in the case of SAR imaging of rain cells, the situation is quite different. As shown in Subsections 3.2, 3.3 and 3.4.1, the co- and cross-polarization NRCS values in the rain cell areas are usually much higher than in the surrounding rain-free areas. Thus the analysis of fully polarimetric SAR data showing radar signatures of rain cells is quite challenging and should not be hampered by signal-to-noise problems as in the case of oil spill detection.

Several polarimetric quantities have been derived from full-polarimetric (quad-polarization) SAR data, among them entropy (H) and mean scattering angle (α) and anisotropy (A), see Appendix. Most often only the entropy and mean scattering angle are used for determining the scattering mechanisms. Figs. 9(a) and 9(b) show maps of entropy and mean scattering angle for a section of the Radarsat-2 image depicted in Fig. 8 around the rain cell. Fig. 9 shows that outside the rain-free areas the values of H and α are quite small indicating Bragg scattering. However, in the areas where the VV and HH NRCS curves (Fig. 8(d)) show peaks due to the presence of rain, H and α are elevated. At the peaks, the maximum values of H and α are 0.5 and 28^{o}, respectively. These values still lie in the section of the H/α diagram indicating surface scattering, see Fig. 1A of the Appendix. According to Lee & Pottier (2009), H values above 0.4 indicate contributions from second order and higher order surface scattering. Thus we conclude from the polarimetric decomposition shown in Fig. 9 that surface scattering is the dominant scattering mechanism causing the radar signature of this rain cell, but there are also non-Bragg scattering (higher order scattering) contributions.

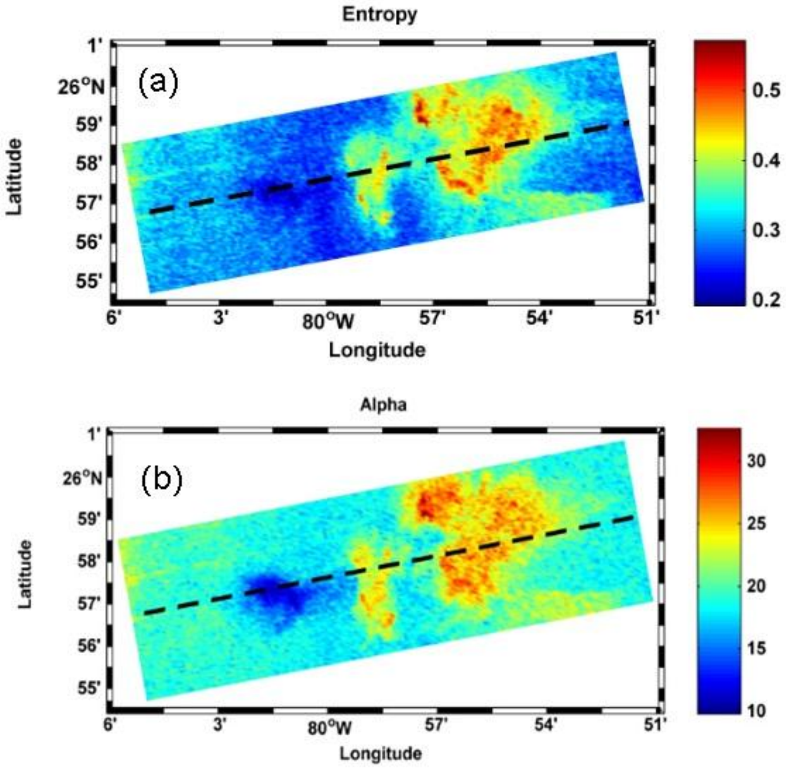

Fig. 9. Maps of (a) entropy and (b) mean scattering angle of the area around the rain cell visible on the Radarsat-2 image depicted in Fig. 8.

3.5. Envisat ASAR images

In the previous subsections we have focused on studying the radar signatures of individual rain cells with the aim of identifying the physical mechanism causing the observed radar signatures. In this subsection we present examples showing that C-band radar signatures of rain are quite variable. They can consists of areas of enhanced, reduced, or enhanced/reduced NRCS values relative to the background depending on rain rate, drop size distribution, wind speed, and time evolution of the rain event. In all cases shown, we have checked the radar signatures of rain observed on the Envisat ASAR images by concurrent weather radar images. First we present two ASAR images showing rain events in low wind areas where the NRCS is enhanced and then two ASAR images showing rain events in high wind areas where the NRCS is reduced. Finally, we present an ASAR image of a rain band (convective rain) where the NRCS is partly increased and partly decreased.

3.5.1. Case of rain with moderate rain rate in a low wind speed environment

Fig. 10(a) shows an Envisat ASAR image which was acquired in the Alternating Polarization (AP) Mode at VV and VH polarizations (incidence angle: 33.55^o - 36.05^o) on 20 April 2003 at 01:55 UTC over the Taiwan Strait west of Taiwan showing a rain event. A weather radar image acquired on the same day at 02:00 UTC provided by the Central Weather Bureau of Taiwan is shown in Fig. 10(b). One would not immediately recognize that the patchy bright areas on the SAR image are radar signatures of rain. Indeed, we first also misinterpreted these bright features (as radar signatures of a macro-algae bloom), but the weather radar image then revealed that it resulted from stratiform rain. Fig. 11 shows the variation of the NRCS at HH and HV polarizations along the transect inserted into the HH polarization SAR image (Fig. 10(a)). The rain rate was 12-24 mm h^{-1} (moderate rain) and the ambient wind was blowing with a speed of 5 m s^{-1} from southeast as given by the atmospheric model of the National Centers for Environmental Prediction (NCEP). The NRCS at HH polarization increases in the rain area by 4 to 8 dB, while at HV polarization the NRCS increases only by up to 2 dB. However, these measured NRCS values at cross-polarization are not very reliable because they lie near the noise level of the instrument. According to the Scheuchl & Cumming (2005), the NESZ at HV polarization lies at an incidence angle of 35^o incidence for Envisat ASAR around -22.5 dB.

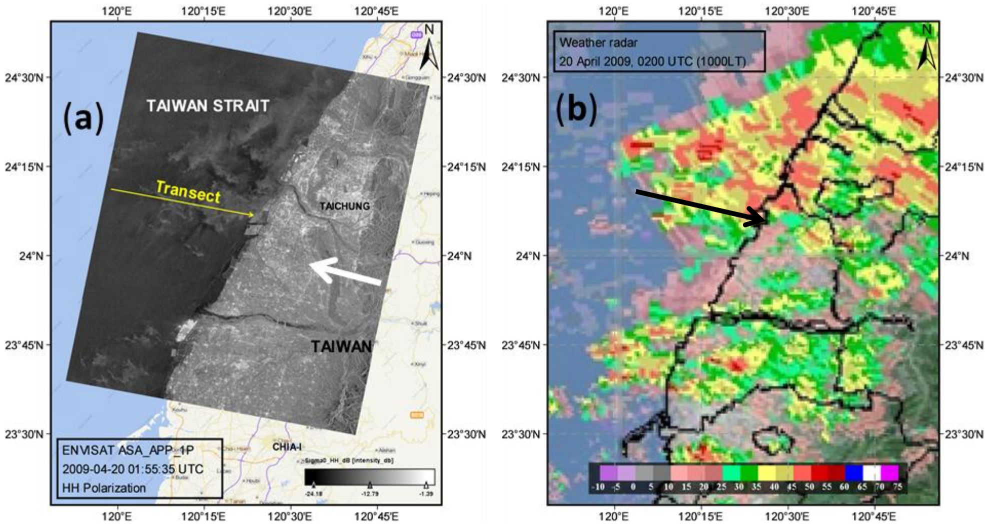

Fig. 10. (a) Envisat ASAR image acquired in the Alternating Polarization Mode at HH polarizations during a descending satellite path over the Taiwan Strait west of Taiwan on 20 April 2009 at 01:55 UTC showing radar signatures of rain. Inserted is the look direction of the SAR antenna (thick white arrow) and the transect along which the variations of the NRCS at HH and HV polarizations has been determined, see Fig. 11. (b) Weather radar image acquired on 20 April 2009 at 02:00 UTC (10:00 LT). The rain rate was 12-24 mm h^{-1} as and the ambient wind was 5 m s^{-1} from southeast.

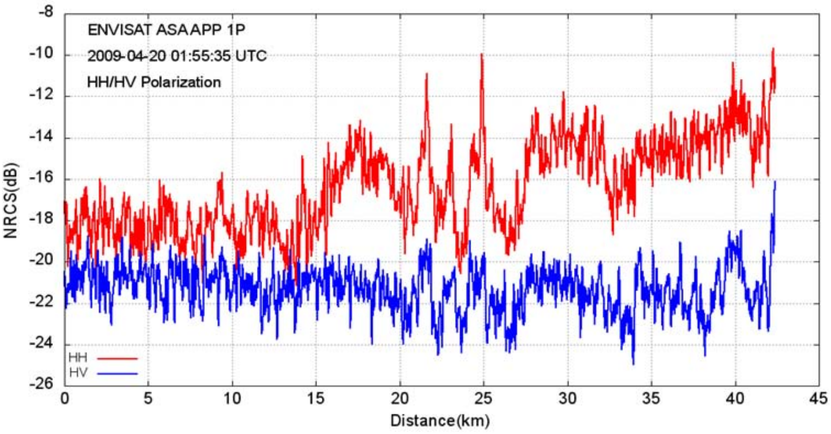

Fig. 11. Variation of the NRCS at HH and HV polarizations along the transect inserted into the Envisat dual polarization ASAR image depicted in Fig. 10(a).

3.5.2. Case of rain with high rain rate in a low wind speed environment

Fig. 12 shows an Envisat ASAR image acquired in the Image Mode (100 km swath width) at VV polarization on 16 June 2008 at 14:22 UTC over the Pearl River delta (west of Hong Kong) together with the weather radar image acquired on the same day at 14:18 UTC (22:18 LT) by the Hong Kong Observatory. They show an extended rain area with rain rates between 10 and 50 mm h^{-1}. A weak ambient wind with a speed of 2-4 m s^{-1} was blowing from southeast as given by the NCEP model. A close inspection of the SAR image reveals that the rain area has a quite inhomogeneous texture (variation of the NRCS by +/- 1 dB) and that there are small, slightly bright patches at the rim of the rain area. Also in this case, the NRCS is increased in the rain area. In the adjacent area south of the rain area is visible also an area of increased NRCS, but there is no rain. In this case it is due to downdraft winds from rain cells located further south, see Fig. 12(b).

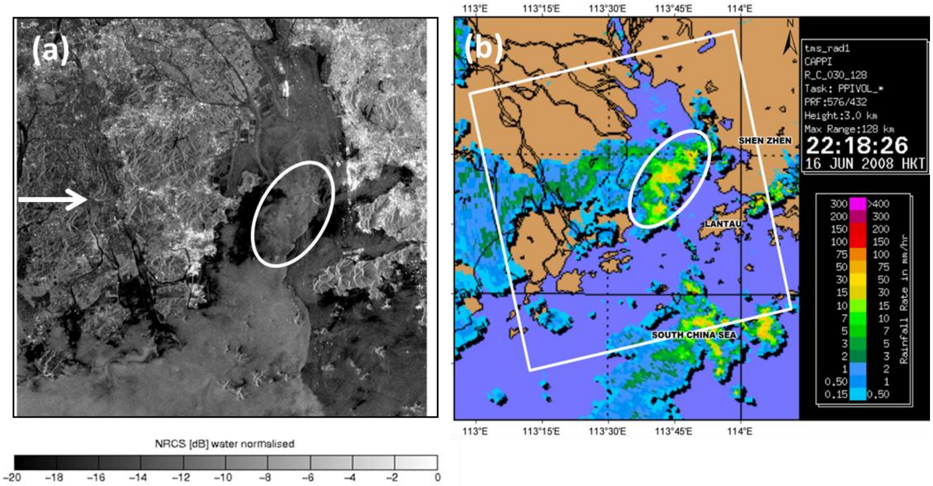

Fig. 12. (a) Envisat ASAR image acquired in the Image Mode (100 km swath width) at VV polarization over the Pearl River delta on 16 June 2008 at 14:22 UTC showing the radar signature of a large rain area located in the Pearl River delta (inside the white ellipse) as a bright area. The white arrow denotes the look direction of the SAR antenna. (b) Weather radar image of the Hong Kong Observatory acquired on 16 June 2008 at 14:18 UTC (22:18 LT). The rain rate in the circled region varied between 10 and 50 mm h^{-1} and the ambient wind was 2-4 m s^{-1} from southeast.

3.5.3. *Case of a squall line with high rain rate in a high wind speed environment*

Fig. 13 shows an Envisat VV polarization ASAR image acquired on 6 August 2008 over the South China Sea off the coast of Hong Kong on 6 August 2008 at 14:18 UTC together with the weather radar image acquired on the same day at 14:18 UTC (22:18 LT) by the Hong Kong Observatory. They show the radar signature of a squall line in which the rain rate varied between 30 and 75 mm h^{-1}. A strong ambient wind with a speed of 12-14 m s^{-1} was blowing from southeast as given by the NCEP model. Here the radar signature consists mainly of areas of reduced NRCS values caused by wave damping due to turbulence. A

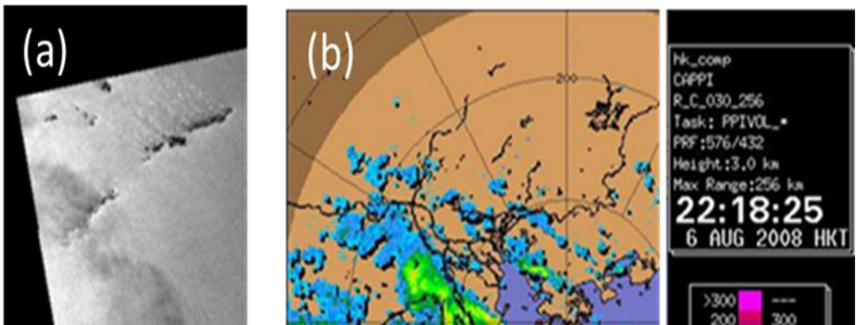

scan along a transect crossing the dark band (not reproduced here) shows a reduction of the NRCS by 1.8 dB.

Fig. 13. (a) Envisat ASAR VV polarization image acquired in the Image Mode over the South China Sea off the coast of Hong Kong on 6 August 2008 at 14:18 UTC showing radar signatures of a squall line. (b) Weather radar image of the Hong Kong Observatory acquired on 6 August 2008 at 14:18 UTC (22:18 LT). Here the squall line appears in the SAR image as an area of predominantly reduced NRCS (dark grey tone in the image). The rain rate in the squall line varied between 30 and 75 mm h^{-1} (heavy rain) and the ambient wind was 12-14 m s^{-1} from southeast.

3.5.4. Case of rain with low rain rate in a high wind speed environment

Fig. 14(a) shows an Envisat HH polarization ASAR image acquired on 9 December 2011 at 21:18 UTC in the Wide Swath Mode the southern North Sea and Fig. 14(b) the weather radar image acquired on the same day at 21:15 UTC (22:15 LT) by the German Weather Service (DWD). They show a large area of stratified rain with light to moderate rain rates (1 to 5 mm h^{-1}). Fig. 15(a) shows a strong ambient wind with a speed of 12-14 m s^{-1} was blowing from northwest as given by the NCEP model. This SAR image has in the rain area a quite inhomogeneous texture with variations of the NRCS by up to 4 dB. The radar signature consists mainly of areas of reduced NRCS values caused by wave damping due to turbulence, but also of some areas of increased NRCS values relative to the background, which we attribute to downdraft winds. Fig. 15(a) shows the surface wind field as given by the NCEP model and Fig.15(b) the sea surface wind field derived from the ASAR image using the C-band Wind Scatterometer Model Function version 4 (CMOD4; Stoffelen & Anderson, 1997) and the wind direction given by the NCEP model valid for 21:00 UTC. The ASAR image (Fig. 14(a)) shows in the rain area mainly areas of reduced NRCS intermixed with areas of enhanced NRCS. Comparing the NCEP winds (Fig. 15(a)) and the SAR-derived winds (Fig. 15(b)), one can see that the reduction dominates leading to an apparent reduction in wind speed in the rain area.

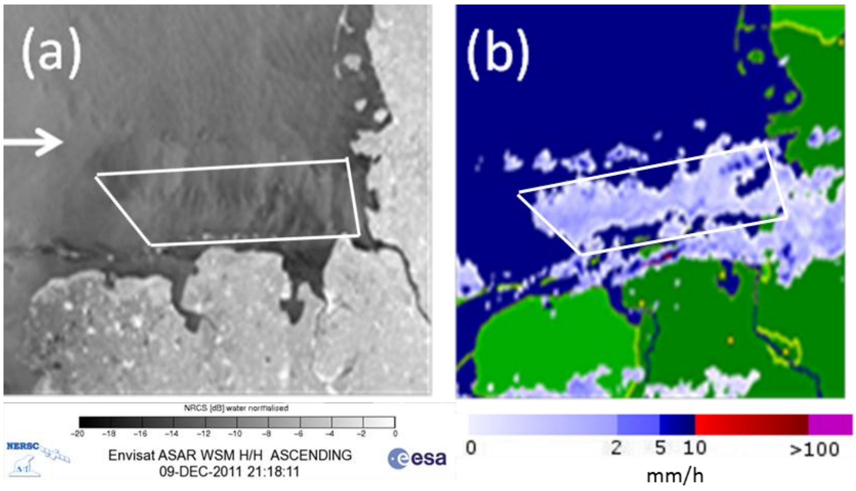

Fig. 14. (a) Envisat ASAR image acquired in the Wide Swath Mode (405 km swath width) at HH polarization over the southern North Sea on 9 December 2011 at 21:18 UTC showing the radar signature of a broad rain area. The white arrow denotes the look direction of the SAR antenna. (b) Weather radar image of the German Weather Service acquired on 9 December 2011 at 21:15 UTC (22:15 LT). The rain rate in the area marked by a white rhombus varied between 1 and 5 mm h^{-1} and the ambient wind was 12-14 m s^{-1} from northwest.

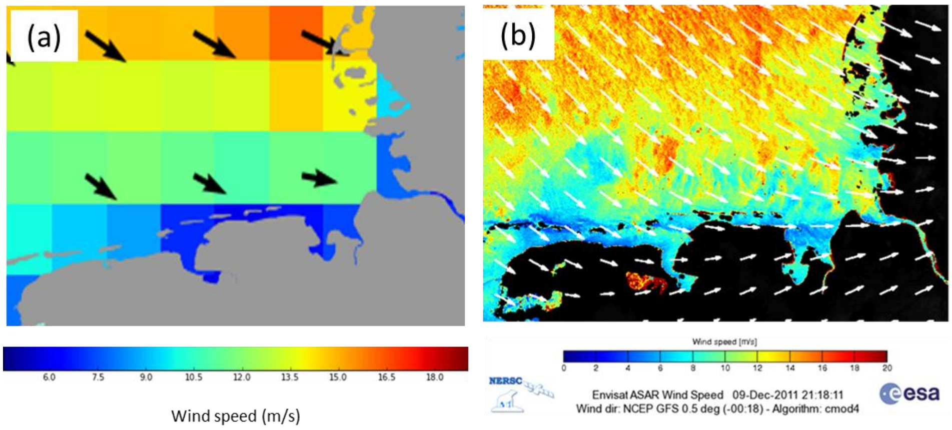

Fig. 15. (a) Wind field given by the NCEP model, valid for 9 December 2011 at 21:00 UTC; (b) Wind field retrieved from the Envisat ASAR image depicted in Fig. 14(a) by using the wind direction from the NCEP model valid for 9 December 2011at 21:00 UTC. The arrows over land denote the wind direction as given by the NCEP model.

3.5.5. Case of a rain band with high rain rate in a low wind speed environment

Fig. 16 shows an Envisat ASAR image acquired on 18 August 20112011 at 02:27 UTC in the Wide Swath Mode (swath width: 405 km) over the South China Sea south of Hong Kong on which a rain band along a weak wind front (in the center) is visible and also several rain cells (in the lower left section). The incidence angle range is from 16^{o} to 42^{o}. Note that the look direction of the SAR antenna is from the left (thick white arrow) such that the dark areas cannot result from shadowing as discussed in Section 2.2 (Fig. 3(a)). Instead, we interpret the dark patches as being caused by attenuation of the C-band Bragg scattering waves by the rain-induced turbulence. The time series of the weather radar images show that the rain band was moving westward with a speed of approximately 33 km h^{-1}. Thus part of the dark patches may still result from damping of the Bragg waves by turbulence after it has stopped raining. A weak ambient wind with a speed of 2-4 m s^{-1} was blowing from east as given by the NCEP model. We interpret the bright patches as being caused by scattering at ring waves and partly also by scattering at splash products.

Fig. 17(a) shows the weather radar image acquired on 18 August 2011 at 02:24 UTC (10:24 LT) by the Hong Kong Observatory and Fig. 17(b) the vertical profile of the reflectivity along the transect inserted in Fig. 17(a). The rain rate was up to 50 mm h^{-1}. Note that there is no melting layer and that in this weather radar image the radar reflectivity is quite variable in the horizontal as well as in the vertical direction.

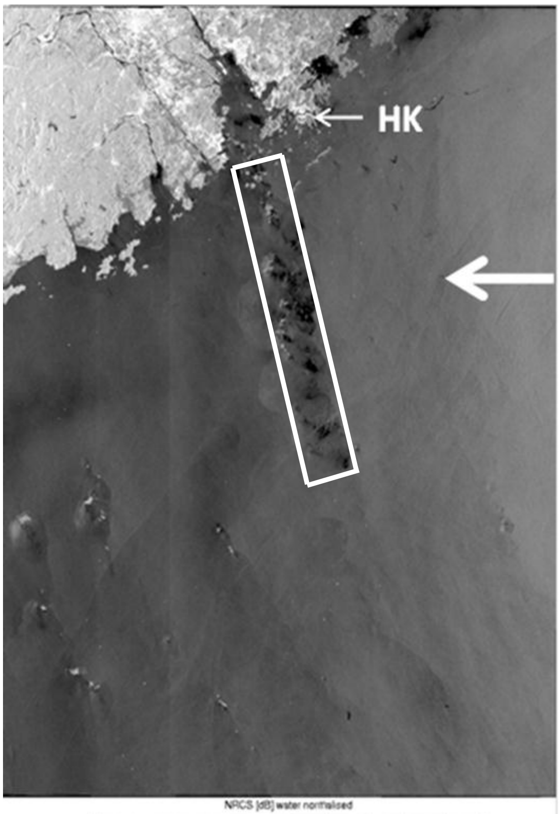

Fig. 16. Envisat ASAR images acquired in the Wide Swath Mode (WSM) at VV polarizations during a descending satellite path over the South China Sea south of Hong Kong on 18 August 2011 at 02:27 UTC showing the radar signature of a rain band (inside the inserted rhombus). Inserted in the image are the look direction of the SAR antenna (thick white arrow) and the location of Hong Kong (HK). The rain rate in the rain band was up to 50 mm h^{-1} and the ambient wind was 2-4 ms^{-1} from east.

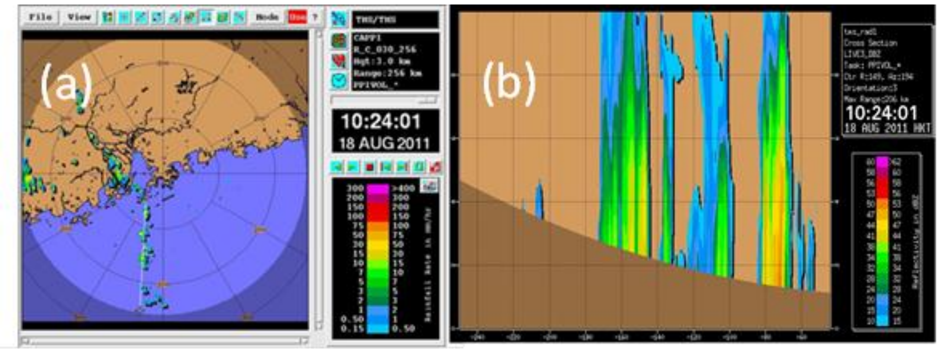

Fig. 17. (a) Weather radar image acquired on 18 August 2011 at 02:24 UTC (10:24 LT), 3 minutes before the ASAR image depicted in Fig. 16 was acquired, It shows a rain band stretching south into the South China Sea, which is also visible in Fig. 16 inside the inserted white rhombus. (b) Vertical profile of the radar reflectivity along a transect through the rain band visible in Panel (a).

4. Effect of rain on C-band scatterometer data

The effect of rain on C-band scatterometer data has been investigated by Nie and Long (2007) using data of the wind scatterometer of the Active Microwave Instrument (AMI) onboard the European Remote Sensing (ERS) satellites, and by Lin et al. (2013) using data of the Advanced Scatterometer (ASCAT) onboard the European MetOp satellites. Note, that the spatial resolution of scatterometers is much larger than of SARs, typically 25 km x 25 km. For estimating rainfall, Nie and Long (2007) used data of the Tropical Rainfall Mission's (TRMM) Precipitation Radar (PR). They found that the rain-induced C-band NRCS increases with rain rate and that the effect of rain has a more significant impact on the measurements at high incidence angles than at low incidence angles. This is in accordance with our findings that the rain-induced enhancement of the NRCS increases with Bragg wavenumber (see Fig. 2).

The increase of the C-band NRCS with rain rate is also evident in ASCAT data as shown by Lin et al. (2013), see Fig.18. They were running the Wind Data Processor of the European

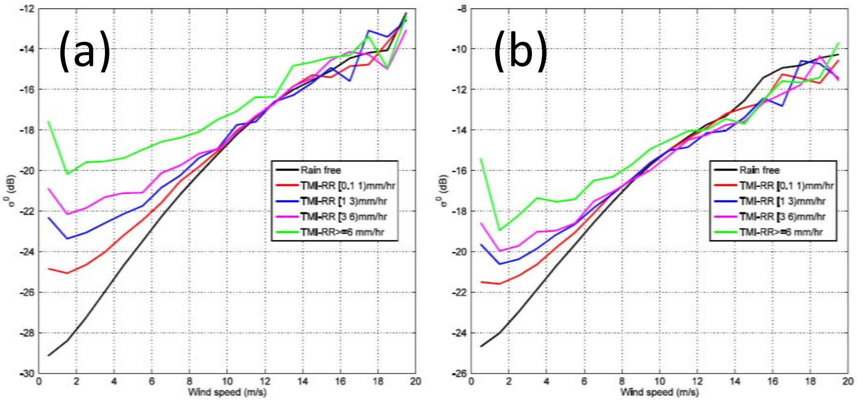

Fig. 18. C-band area-mean NRCS (σ^o) retrieved from ASCAT data (VV polarization) as a function of wind speed for different rain rates for different Wind Vector Cells (WVC) (a) WVC-mean NRCS for WVC number 11 measured by the fore-beam at an incidence angle of 52.8°; (b) Same, but measured by the mid-beam at an incidence of 41.7°. Reproduced from Lin et al. (2013).

Organization for the Exploitation of Meteorological Satellites (EUMETSAT) for 6 months, with and without the rain correction model, and using for validation collocated rain data of the Microwave Imager (TMI) of TRMM and model winds from the European Centre for Medium Range Weather Forecasts (ECMWF). Fig. 18 shows the mean NRCS from the Wind Vector Cell (WVC) number 11 as a function of wind speed for different rain rates. In order to retrieve two-dimensional wind fields, ASCAT measures the radar backscattering of a cell on the sea surface from three different directions by three beams: the fore-beam, the mid-beam, and the aft-beam, which are separated by 45° in azimuth. In Fig. 18(a) and Fig. 18(b) are depicted the data from the fore-beam and the mid-beam, which, for WVC 11, have incidence angles of 52.8° and 41.7°, respectively. The plots show that the rain-induced C-band NRCS (difference between the total NRCS and the NRCS in the absence of rain) increases with rain rate, but decreases with wind speed. At a wind speed of about 12 m s^{-1}, the impact of rain on the NRCS is close to zero. In particular Fig. 18(b) shows that above 14 m s^{-1}, the impact of rain on the NRCS becomes negative, i.e., rain reduces the NRCS. Note that the data plotted in Fig, 18(b) are mid-beam data, i.e., the data are captured at a higher incidence angle (41.7°) than the data from the fore-beam (52.8 °). Since the radar backscattering from the mid-beam is caused by Bragg waves with longer wavelengths (see Eq. (1)), damping of the Bragg waves by rain-induced turbulence is stronger at lower incidence angles, which agrees with the findings presented in Section 2.1.

However, some care has to be taken when interpreting on C-band scatterometer data with respect to rain effects. Since scatterometers have a much coarser resolution than SARs, they cannot resolve individual rain cells. Some of the observed variations in NRCS may be due to an increase of in wind speed due to downdrafts associated with rain cells and not due to an increase of the sea surface roughness caused by scattering at ring waves or splash products (Portabella, private communication).

5. Discussion

The radar signatures of rain are particularly complex at C-band, and it is often difficult to identify features visible on C-band SAR images as radar signatures of rain. Rain cells can be easily identified on C-band SAR images of the sea surface when they are associated with downdraft, i.e., with wind roughening the sea surface. But rain cells are not always accompanied by downdraft. Rain becomes visible on C-band radar images of the ocean also because the impinging rain drops (1) generate ring waves and thereby increase the small-scale sea surface roughness and thus the radar backscatter, (2) generate turbulence in the upper water layer and thereby decrease the sea surface roughness and thus the radar backscatter, and (3) generate splash products consisting of stalks, craters, crowns, and rain drops bouncing upwards which also causes increase of radar backscattering. However, details of this last scattering mechanism await further investigations. Usually it is assumed that scattering and attenuation of the radar beam by rain drops in the atmosphere do not contribute to the C-band radar signature of rain over the ocean at all rain rates. But Envisat ASAR images acquired over the South American rain forest, one of which is shown in Fig. 3, and an ERS-1 SAR image acquired over the coastal waters south of Singapore, which was analyzed in the paper by Lin et al. (2001), prove that this assumption is not true. However, we expect that scattering and attenuation by rain drops in the atmosphere becomes a significant factor in C-band radar signatures of rain over the ocean only when the rain rate is very high (>50 mm h^{-1}). Unfortunately, we have found in the archives of ESA and CSA no C-band SAR images acquired over the ocean, on which radar signatures of rain cells, like the one visible on the Envisat ASAR image acquired over the South American rain forest (Fig. 3(a)), can be delineated. This is probably due to the fact that rain events with very high rain rates (>50 mm h^{-1}) are very rare events and the probability to capture them by spaceborne SARs is very low. On the other hand, bright patches associated with rain cells have been observed occasionally on X-band SAR images, but there they are caused by scattering at raindrops in atmosphere.

Polarimetric decomposition analysis of the Radarsat-2 image shown in Fig. 8 has yielded the result that surface scattering is the only mechanism causing the radar signature of this rain cell imaged by Radarsat-2 and that also higher order surface scattering mechanisms are involved.

In the analysis of SAR images acquired by the C-band SAR onboard the spaceshuttle Endeavor during the SIR-C/X-SAR mission and onboard the Envisat and Radarsat-2 satellites, we have observed strong increases of the NRCS at co- and cross-polarizations in rain cell areas. One possible explanation is scattering at splash products as proposed by Atlas (1994) and Wetzel (1990). But also other scattering mechanisms have been proposed. One of them is the direct-reflected scattering mechanism proposed by Jameson et al. (1997), in which the microwaves are reflected at the sea surface and then scattered by raindrops above the sea surface. A similar mechanism has been invoked by Durden et al. (1989) and Chauhan et al. (1991) to explain the often measured large co-polarized radar return from vegetation. In this case, the radar pulse is reflected by the rough soil surface and scattered at leaves and stalks. Also low-salinity "puddles" in the upper water layer generated by heavy rain as suggested by Wijesekera & Gregg (1996) might contribute to the scattering mechanism since the penetration depth of the microwaves in freshwater is larger than in salt water, and volume scattering by density inhomogeneity in water can cause depolarization (Valenzuela, 1978). Another mechanism could be scattering at steep slopes at the rim of the craters generated by the impinging rain drops.

Finally, we would like to draw the attention of the reader to the similarity of the radar signature of rain over the South American rain forest visible in Fig. 3(b) and the bright section within the radar signature of the rain cell over the ocean visible in Fig. 6 and 7. One could speculate that the underlying scattering mechanisms are similar: (1) scattering of the radar pulse at leaves, twigs or stalks of the trees and then interacting resonantly with rain drops reflected by them and (2) scattering of the impinging radar pulse at the rough sea surface and then interacting resonantly with rain drops bouncing upwards. However, the polarimetric decomposition analysis presented in Section 3.4.2 does not support this interpretation.

6. Summary

Rain over the ocean affects the radar backscatter, which is of importance for retrieving sea surface wind information from scatterometer data and for determining the origin of features visible on SAR images of the sea surface correctly. This paper has been aimed at identifying the physical mechanisms causing C-band radar signatures of rain over the ocean. C-band radar signatures are especially complex because they get contributions from several scatter and attenuation mechanisms. The main parameters determining the C-band radar signatures of rain over the ocean are rain rate and wind speed. A puzzling observation is that rain cells manifest themselves on C-band SAR images often as bright patches caused by a strong increase of the co-polarized radar backscatter, which is accompanied by a strong increase of the cross-polarized radar backscatter.

In order to get an insight into scattering mechanisms causing the observed C-band radar signatures of rain over the ocean, we have resorted to laboratory and field measurements carried out more than 15 years ago in the US (NASA's Wallops Flight Facility) and Germany (University of Hamburg). Furthermore, we have resorted to space-borne SAR data acquired by the L-band SAR on Seasat (1978) and the X-, C-, and L-band multi-polarization SAR flown on a spaceshuttle during the SIR-C/X-SAR mission in 1994. An example of a multi-frequency/ multi-polarization SIR-C/X-SAR SAR image of a rain cell in the Gulf of Mexico is depicted in Fig. 5. It shows that the radar signature of a rain cell depends strongly on radar frequency and polarization. Then we have analyzed radar signatures of rain cells visible on a dual-polarization (VV and VH) Sentinel-1A SAR image and on a quad-polarization (VV, HH, VH, and HV) Radarsat-2 image. Finally, we presented 5 representative Envisat ASAR images of rain events over the ocean together with collocated weather radar images, which support our interferences on the origin of C-band radar signatures of rain over the ocean.

We conclude from a synopsis of results obtained from laboratory and field measurements and from the analysis of space-borne SAR images showing radar signatures of rain over the ocean the following:

1) C-band radar signatures of rain can be positive or negative, i.e., the NRCS can be enhanced or reduced relative to the background. Enhancement is caused by scattering at ring waves and splash products generated by rain drops impinging onto the sea surface and by downdraft winds associated with rain cells. Reduction is caused by attenuation of the Bragg waves due to turbulence generated by the rain drops impinging onto the sea surface. Whether the NRCS is enhanced or reduced depends on rain rate, wind speed, incidence angle, rain drop distribution, and history of the rain event. We were unable to give quantitative results about these dependencies on these parameters, because of the limited data set and the variability of rain events. However, we were able extract the following trends:

   a) At low to medium ambient winds (< 10 m s^{-1}) and low to medium rain rates (< 50 mm h^{-1}), Bragg scattering at ring waves and scattering at splash products are the dominating contributors to the C-band radar signature of rain causing enhancement of the NRCS. Since the maximum of the ring wave spectrum lies in range of the wavelengths of C-band Bragg waves, C-band radars are particularly responsive to ring waves (Fig. 2). The spectrum of the ring waves increases with rain rate (Fig. 1), which implies that, according to Bragg scattering theory, also the NRCS increases with rain rate. This agrees with statistical analyses carried out by Lin et al. (2013) using ASCAT, TRMM/TMI, and model wind data.

   b) At high ambient winds (>10 m s^{-1}) and at low to high rain rates (but < 50 mm h^{-1}), rain causes reduction of the C-band NRCS relative to the background. The higher the rain rate, the stronger is the reduction. We attribute this to the damping to turbulence generated by the impinging rain drops.

   Typical measured values for the variation of the C-band NRCS due to rain are: -3 dB < σ^{o}_{rain} < +7 dB. At L-band, where the Bragg waves have wavelengths around 25 cm, damping of ring waves by turbulence always dominates, which implies that the NRCS in rain areas is always reduced relative to the background. However, at L-band, like at all other radar bands, the NRCS increases when downdraft winds are present.

2. At C-band, the sensitivity to rain increases with increasing incidence angle. This can be explained by the fact that the Bragg wavelength decreases with incidence angle (see Eq. (1)). The shorter the Bragg wavelength, the stronger is the scattering at ring waves leading to an enhancement of the NRCS. This agrees with the findings of Nie and Long (2007) and Lin et al. (2013), see Fig. 18.
3. Since, in general, the rain rate varies spatially and temporally during a rain event, C-band radar signatures of rain often consists of adjacent areas of enhanced and reduced NRCS values (relative to the ambient rain-free and downdraft-free area). At the initial stage of the rain event, the turbulence in the upper water layer is not fully developed and thus its damping effect on the water waves is small. On the other hand, after it has stopped raining, the turbulence does not decay immediately (the lifetime of the turbulence is on the order of a minute) and it keeps damping the Bragg waves even after it has stopped raining.
4. At very high rain rates (probably above 50 mm h^{-1}) scattering and attenuation of the radar pulse by rain drops in the atmosphere can also contribute to the C-band radar signatures of rain. This has been inferred from Envisat ASAR images acquired over the South American rain forest (Fig. 3(a)). We have speculated that bright patches, which are often visible on C-band SAR images of tropical rain forests and not accompanied by dark shadows, result from scattering at the melting layer (Fig. 3(b)).
5. The bright patches often observed in C-band co-polarized SAR images in downdraft patterns (see Figs. 4, 6, 7, 8), but also at wind fronts (see Fig. 3 in Alpers et al., 2012 and Fig. 6 in Alpers et al., 2015) are caused by surface scattering. The strongest argument in support of this hypothesis comes from L-band Seasat SAR images, on which occasionally also such bright patches are observed (Fig. 4). The long wavelength of the Seasat SAR (23.5 cm) precludes that the bright patches are caused by volume scattering by raindrops in the atmosphere. Also the polarimetric decomposition analysis of a Radarsar-2 image of a rain cell supports the surface scattering hypothesis.

6. The scattering mechanism causing the bright patches in C-band, co-polarized SAR images of rain cells could not be determined. It must be associated with a non-Bragg scattering mechanism since the co-polarized radar signatures of rain cells are approximately equal (Fig. 8(d)) and the large co-polarized radar signatures of rain cells are always accompanied by a large cross-polarization radar signature (Figs. 6, 7, 8). One possible explanation is scattering at splash products as proposed by Atlas (1994), but also other mechanism have been proposed: 1) reflection of the microwave at the sea surface and then scattered by raindrops above the sea surface, 2) scattering at low-salinity "puddles" in the upper water layer generated by heavy rain, and 3) scattering at steep slopes at the rim of the craters generated by the impinging rain drops.
7. It is very unlikely that the strong increase of the cross-polarized NRCS in rain cells areas is caused by an instrumental effect, i.e., by crosstalk between the co-polarized and cross-polarized channels. At least, this can be excluded for Radarsat-2, where the inter-channel crosstalk is better than -45 dB (Vachon & Wolfe, 2011). This value is much lower than the lowest measured cross-polarized NRCS (-32 dB) in the Radarsat-2 scene depicted in Fig. 8.

Although we could not present a quantitative theory explaining the observed C-band radar signatures of rain, we hope that the synopsis of data from laboratory and field measurements and from the analysis of space-borne SAR data presented in this paper will be helpful for remote scientists to better identify radar signatures of rain on C-band SAR images of the sea surface. Furthermore, we hope that they will help in developing a quantitative theory of C-band radar signatures of rain over the ocean. There is a pressing demand for such a theory since many C-band SARs and scatterometers will be flying in space in the near future, the data of which will be used to retrieve near surface winds over the ocean. Rain is a main source of error in these data, especially when co- and cross-polarized data are used together in wind retrieval algorithms.

Acknowledgments

We thank ESA for providing the ERS and Envisat ASAR images free of charge within the ESA/NRSCC (China) DRAGON 3 project, I-I Lin of the National Taiwan University for providing the weather radar image of 20 April 2009, NERSC in Bergen for giving us access to their Envisat ASAR archive and for providing the SAR-derived wind fields. The Sentinel-1A data were provided by the Copernicus program of the European Commission. Many thanks go also to the three anonymous reviewers for very constructive suggestions for improving the paper, to Morten Wegeland Hansen of NRSC for providing the NCEP winds, and to Marcos Portabella of ICM, Barcelona, for valuable comments on the interpretation of the ASCAT data. This study was supported by National Science Foundation of Jiangsu Province Excellent Young Scholar, Grant BK20160090, and National Science Foundation of China for Outstanding Young Scientist, Grant 41622604, and Chinese National High Technology Research and Development (863) program, Grant 2013AA09A505, and the Program for Jiangsu Province Innovative Research Team, and by the ESA, Contracts No. 4000115170/15/I-SBo (SEOM S1-4SCI Ocean Study) and No. 4000107360/12/I-LG (Sentinel-1A Mission Performance Center.

References

Alpers, W., & Melsheimer, Ch. (2004). “Rainfall", Chapter 17 in *Synthetic Aperture Radar Marine User's Manual*, NOAA/NESDIS, Ch. R. Jackson, J.R. Apel, editors, Washington, D.C., USA, ISBN 0-16-073214-X, 355-37. Available online: http://www.sarusersmanual.

Alpers W., Wong, W. K., Dagestad, K.-F, & Chan, P. W. (2012). A northerly winter monsoon surge over the South China Sea studied by remote sensing and a numerical model. *International Journal of Remote Sensing*, *33*, 7361–7381. doi: 10.1080/01431161.2012.685983.

Code de champ modifié

Alpers, W., Wong, W. K., Dagestad, K.-F., & Chan, P. W. (2015). Study of a wind front over the Northern South China Sea generated by the freshening of the North-East Monsoon. *Boundary- Layer Meteorology*, *157*, 125-140, doi: 10.1007/s10546-015-0050-8.

Atlas, D. (1994). Origin of storm footprints on the sea seen by synthetic aperture radar. *Science*. *266*, 1364-1366.

Behan, A., & Woodhouse, E. (1999). Synthetic aperture radar polarimetry for forestry applications, Survey Ireland - Winter 1999. Available on-line: https://www.dit.ie/media/built/images/spatialplanning/SARSI.pdf.

Bliven, L., Branger, H., Sobieski, P., & Giovanangeli, J.-P. (1993). An analysis of scatterometer returns from a water surface agitated by artificial: evidence that ring-waves are the main feature. *International Journal of Remote Sensing*, *14*, 2315-2329.

Bliven , F., Sobieski, P. W., & Craeye, C. (1997). Rain generated ring-waves: measurements and modelling for remote sensing. *International Journal of Remote Sensing*, *18*, 221-228, doi:10.1080/014311697219385.

Braun, N. (2002). Untersuchungen zur Radar-Rückstreuung und Wellendämpfung beregneter Wasseroberflächen, *Ph. D. thesis*, University of Hamburg, Germany.

Braun, N., & Gade, M. (2006). Multifrequency scatterometer measurements on water surfaces agitated by artificial and natural rain. *International Journal of Remote Sensing*, *27*, 27-39.

Braun, N., Gade, M., & Lange, P. A. (2002). The effect of artificial rain on wave spectra and multi-polarization X-band radar backscatter. *International Journal of Remote Sensing*, *23*, 4305–4323.

Chauhan, N. S., Lang, R. H., & Ranson, K. J. (1991). Radar modeling of a boreal forest. *IEEE Transactions on Geoscience and Remote Sensing, 29, 627-638.*

Cloude, S. R., & Pottier, E. (1996). A review of target decomposition theorems in radar polarimetry. IEEE *Transactions on Geoscience and Remote Sensing*, 34, 498-518.

Cloude, S. R., & Pottier, E. (1997). An entropy based classification scheme for land applications of polarimetric SAR. *IEEE Transactions on Geoscience and Remote Sensing, 35*, 68 -78.

Contreras, R. F., Plant, W. J., Keller, W. C., Hayes, K., & Nystuen, J. (2003). Effects of rain on Ku-band backscatter from the ocean. *Journal of Geophysical Research*, *108(C5)*, doi: 10.1029/2001JC001255.

Danklmayer, A., Döring, B. J., Schwerdt, M., & Chandra, M. (2009). Assessment of atmospheric propagation effects in SAR images. *IEEE Transactions on Geoscience and Remote Sensing, 47*, 3507-3518.

Durden, S. L., van Zyl, J. J., & Zebker, H. A. (1989). Modeling and observation of the radar polarization signature of forested areas. *IEEE Transactions on Geoscience and Remote Sensing, 27*, 290-301.

Fu, L., & Holt, B. (1982). Seasat views of the oceans and sea ice with synthetic aperture radar. JPL *Publication 81-120*, Jet Propulsion Laboratory, Pasadena, California, 106–107.

Jameson, A. R., Li, F. K., Durden, S. L., Haddad, Z. S., Holt, B., Fogarty, T., Im, E., & Moore, R .K. (1997). SIR-C/X-SAR observations of rain storms. *Remote Sensing of Environment*, *59*, 267-279.

Jordan, R. L., Huneycutt, B. L., & Werner, W. (1995). The SIRC/X-SAR synthetic aperture radar system. *IEEE Transactions on Geoscience and Remote Sensing*, *33*, 829-839.

Kudryavtsev, V., Hauser, D., Caudal. G., & Chapron, B. (2003). A semi-empirical model of the normalized radar cross-section of the sea surface - 1. Background model. *Journal of Geophysical Research Oceans*, 108(C1), 108 (C3), 8054, doi:10.1029/2001JC001003.

Lee, J.-S. & Pottier, E. (2009). Polarimetric radar imaging, from basics to applications. *CRC Press, Taylor and Francis Group*, 263 pp.

Lemaire, D., Bliven, L. F., Craye, C., & Sobieski, P. (2002). Drop size effects on rain generated ring-waves with a view to remote sensing applications. *International Journal of Remote Sensing*, *23*, 2345–2357.

Lin, I-I, Alpers, W., Khoo, V., Lim, H., Lim, T. K., & Kasilingam, D. (2001). An ERS-1 synthetic aperture radar image of a tropical squall line compared with weather radar data. *IEEE Transactions on Geoscience and Remote Sensing*, 39, 937-945.

Lin, W., Portabella, M., Stoffelen, A., Verhoef, A. Weissman, D., Johnson, T., & Wolf, J. (2013). Towards a correction of ASCAT ocean measurements for rain effects. http://seom.esa.int/LPS13/0d9f3342/ESA_Living_Planet_LIN20130827_MP3.pdf

Lin, W., Portabella, M., Stoffelen, A., Turiel, A., & Verhoef, A. (2014). Rain identification in ASCAT winds using singularity analysis. *IEEE Geoscience and Remote Sensing Letters*, *11*, 1519-1523.

Lin, W., Portabella, M., Stoffelen, A., Verhoef, A., & Turiel, A. (2015). ASCAT wind quality control near rain. *IEEE Transactions on Geoscience and Remote Sensing*, 53 (8), 4165-4177, doi: 10.1109/TGRS.2015.2392372, 2015.

Marshall, J. S., & Palmer, W. M. K. (1948). The distribution of raindrops with size. *Journal of Meteorology,* 5, 165-166.

Melsheimer, Ch. (1998). Signaturen von Regen in Radaraufnahmen des Meeres*, Ph. D. Thesis*, University of Hamburg.

Melsheimer, Ch., Alpers, W., & Gade, M. (1998). Investigation of multi-frequency/multi-polarization radar signatures of rain cells over the ocean using SIR-C/X-SAR data. *Journal of Geophysical Research*, *103*, 18 867-18 884.

Melsheimer, Ch., Alpers, W., & Gade, M. (2001). Simultaneous observations of rain cells over the ocean by the synthetic aperture radar aboard the ERS-1/2 satellites and by weather radars. *Journal of Geophysical Research*, *106*, 4556-4567.

Migliaccio, M., Gambardella, A., & Tranfaglia, M. (2007). SAR polarimetry to observe oil spills. *IEEE Transactions on Geoscience and Remote Sensing, 45, 506-511.*

Migliaccio, M., Nunziata, F., & Gambardella, A. (2009). On the co-polarized phase difference for oil spill observation. *International Journal of Remote Sensing*, *30*, 1587-160.

Minchew, B., Jones, C. E., & Holt, B. (2012). Polarimetric analysis of backscatter from the Deepwater Horizon Oil Spill using L-band synthetic aperture radar. *IEEE Transactions on Geoscience and Remote Sensing,* 50, 3812-3830.

Mouche A., Chapron, B., & Reul, N. (2007). A simplified asymptotic theory for ocean surface electromagnetic wave scattering. *Waves in Random and Complex Media,* 17(3), 321-341. http://doi.org/10.1080/17455030701230261

Nie, C. & Long, D. G. (2007). C-band wind/rain backscatter model. *IEEE Transactions on Geoscience and Remote Sensing, 45, 621-631.*

Ouarzeddine, M., Souissi, B., & Belhadj-Aissa, A. (2007). Classification of polarimetric SAR images base on scattering mechanisms, *5th International Symposium Spatial on Data Quality 2007, Theme: Modelling qualities in space and time*, June 13-15, 2007, ITC, Enschede, The Netherlands, Editor(s): A. Stein, ISPRS Archives – Volume XXXVI-2/C43, 2007, available on-line: http://www.isprs.org/proceedings/XXXVI/2-C43/Postersession/ouarzeddine.pdf

Portabella, M., Stoffelen, A., Lin, W., Turiel, A., Verhoef, A., Verspeek, J., & Ballabrera-Poy, J. (2012). Rain effects on ASCAT-retrieved winds: Toward an improved quality control. *IEEE Transactions on Geoscience and Remote Sensing, 50*, 2495-2506, doi:10.1109/TGRS.2012.2185933.

Pottier, E. (2007). Advanced Training Course on Land Remote Sensing. Available online: http://earth.esa.int/landtraining07/D1LA3-Pottier.pdf.

Pottier, E. (2014). SAR polarimetry, basics. Available online:

http://earth.eo.esa.int/dragon/pottier1_SAR_polarimetry_basics.pdf.

Robinson, I. S. (2004). Measuring the oceans from space: The principles and methods of satellite oceanography, *Springer-Verlag,* Berlin Heidelberg.

Romeiser, R., Alpers, W., & Wismann, V. (1997). An improved composite surface model for the radar backscattering cross section of the ocean surface: 1. Theory of the model and optimization/validation by scatterometer data. *Journal of Geophysical Research: Oceans,* 102**,** 25237-25250. doi: 10.1029/97JC00190.

Scheuchl, B., & Cumming, I. (2005). Analysis of the influence of NESZ variations on cross-polarized signatures of sea ice. *Proceedings of IGARSS 2005*. Available online: sar.ece.ubc.ca/papers/Bernd_IGARSS_2005.pdf

Skrunes, S., Brekke, C., & Eltoft, T. (2014). Characterization of marine surface slicks by RADARSAT-2 multipolarization features. *IEEE Transactions on Geoscience and Remote Sensing, 52*, 5302-5319.

Sobieski, P. W., & Bliven L. F. (1995). Analysis of high speed images of raindrop splash products and Ku-band scatterometer returns. *International Journal of Remote Sensing*, *16*, 2721-2726.

Stoffelen, A., & Anderson, D. (1997). Scatterometer data interpretation: Estimation and validation of the transfer function CMOD4. *Journal of Geophysical Research*, 102, 5767–5780.

Vachon, P. W., & Wolfe, J. (2011). C-band cross-polarization wind speed retrieval. *IEEE Geoscience and Remote Sensing Letters*, *8*, 456-459, doi: 10.1109/LGRS.2010.2085417.

Valenzuela, G. R. (1978). Theories for the interaction of electromagnetic and oceanic waves - A review. *Boundary Layer Meteorology*, *13*, 61-85.

Voronovich, A. G., & Zavorotny, V. U. (2001). Theoretical model for scattering of radar signals from rough sea surface with breaking waves at Ku and C bands, *Waves in Random Media*, 11, 247-269.

Weissman, D. E., Apgar, G., Tongue. J. S., & Bourassa, M. A. (2005). Correcting scatterometer winds by removing rain effects. *Bulletin of the American of Meteorological Society*, *86*, 621-622.

Weissman, D. E., & Bourassa, M. A. (2008). Measurements of the effect of rain-induced sea surface roughness on the QuikSCAT scatterometer radar cross section. *IEEE Transactions on Geoscience and Remote Sensing, 46*, 2882-2894.

Weissman, D. E., & Bourassa, M. A. (2011). The influence of rainfall on scatterometer backscatter within tropical cyclone environments - Implications on parameterization of sea surface stress. *IEEE Transactions on Geoscience and Remote Sensing, 49*, 4805-4814, doi: 10.1109/TGRS.2011.2170842.

Wetzel, L. B. (1990). On the theory of electromagnetic scattering from a raindrop splash. *Radio Science*, *25*, 1183-1197.

Wijesekera, H. W., & Gregg, M. C. (1996). Surface layer response to weak winds, westerly bursts, and rain squalls in the western Pacific Warm Pool. *Journal of Geophysical Research*, *101*, 977- 997.

Worthington, A. M. (1982). A study of splashes. *Proceedings of the Royal Society of London*, 34, 217- 229.

Xu, F., Li, *X.,* Wang, P., & Jin, Y. Q. (2015). A backscattering model of rainfall over rough sea surface for synthetic aperture radar. *IEEE Transactions on Geoscience and Remote Sensing, 53*, 3042-3054.

Zhang, B., Perrie, W., Li, X., & Pichel, W. G. (2011). Mapping sea surface oil slicks using RADARSAT-2 quad-polarization SAR image. *Geophysical Research Letters*, 38, doi:10.1029/2011GL047013.

Appendix

Polarimetric decompostion

Polarimetric SAR measures microwave reflectivity using quad-polarization HH, HV, VH, and VV to form the scattering matrix. In the case of distributed targets, the scattering is described by the coherency or covariance matrix. Measurement of the full scattering matrix allows the identification and/or separation of different scattering mechanisms occurring inside the same resolution cell. Polarimetric decompostion parameters are derived from these second order matrices and from them radar observables, like (polarimetric) entropy (H), mean scattering angle (α), and anisotropy (A). (For an extended review the reader is referred to the book of Lee & Pottier, 2009 and Pottier, 2014). Most often only the entropy and mean scattering angle are used for determining the scattering mechanisms. A diagram showing the different scattering mechanisms in H/ α space, which is widely used in polarimetric studies of land surfaces (see, e.g., Lee & Pottier, 2009; Ouarzeddine et al., 2007), is depicted in Fig. A1. H is a measure for the randomness of the scattering process and takes values between 0 and 1. Small values of H indicate that surface scattering mechanism is dominant. The mean scattering angle α takes values between 0^o and 90^o. It is used as an indicator of the dominating scattering mechanism. When α is small, the scattering mechanism is Bragg scattering, and when α is large, double bounce scattering is present (Zhang et al., 2011; Skrunes et al., 2014). When the entropy increases, the number of identifiable scattering mechanisms decreases. The most common elementary scattering mechanisms are surface, dihedral and volume (or multiple) scattering.

Anisotropy (A) can only be employed as a source for discrimination when H ≥ 0.7 (Lee & Pottier, 2009). Since in our case H ≤ 0.7, we need not to consider A. The H and α maps depicted in Fig. 9(a) and 9(b) show that H is everywhere smaller than 0.5 and α is smaller than 30°, which implies that the scattering falls into Section 7 of Fig. A1, which indicates that the scattering mechanism is surface scattering.

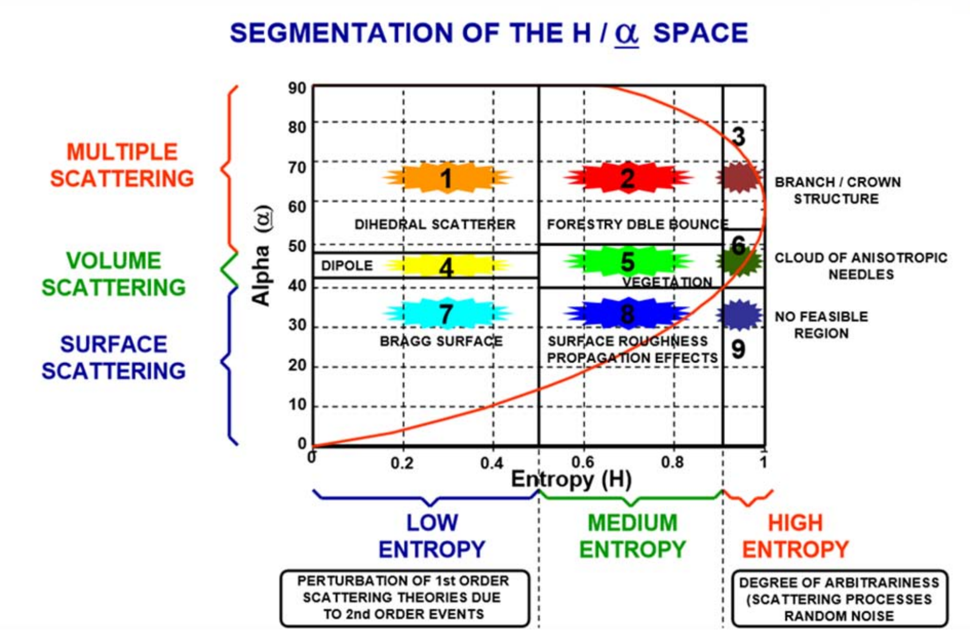

Fig. A1. Scattering mechanism as identified in the H/α plane. Reproduced from Pottier (2007).

Figure captions:

Fig. 1. Ring wave frequency spectrum as measured in the laboratory for rain rates of 5 (dotted line), 50 (dashed line), and 200 mm h^{-1} (solid line). The peak of all three spectra is located around 5.7 Hz. corresponding a wavelength of 5.3

cm. The inserted thick horizontal line at the bottom marks the frequency range of those ring waves which serve as Bragg waves in C-band radar backscattering. Reproduced from Bliven et al. (1997).

Fig. 2. Variation of the NRCS of ocean areas struck by rain as a function of Bragg wavenumber as inferred from data acquired by S-, C-, and X-band, multi-polarization scatterometers mounted on a shore-based tower. Plotted is the ratio of the NRCS at VV polarization in the presence of rain and in the absence of rain as a function of the Bragg wavenumber. The solid line denotes a linear regression to the data, and the dotted lines denote the limits of the 95% confidence interval of this regression. Reproduced from Braun & Gade (2006).

Fig. 3. (a) C-band SAR image acquired by the Advanced SAR (ASAR) onboard the Envisat satellite at VV polarization in the Image Mode (IM) (100 km swath width) during a descending satellite passes over the South American rain forest (a) on 24 April 2010 at 13:51 UTC and (b) on 10 February 2010 at 13:43 UTC. The inset black arrows denote the look direction of the SAR antenna. Note that in image (a) the bright patch is followed to the left by an adjacent dark patch caused by shadowing, while in image (b) no adjacent dark patches (shadows) are visible.

Fig. 4. (a) Schematic sketch of the downdraft of a rain cell spreading over the sea surface where it causes roughening of the sea surface (adapted from Atlas, 1994); (b) Seasat SAR image acquired over the Gulf of Mexico on 11 September 1978 at 17:14 UTC showing at the upper left an elliptically-shaped bright downdraft pattern with a black area in the center, which contains a small bright patch. Adapted from Fu & Holt (1982).

Fig. 5. Multi-frequency, multi-polarization SIR-C/X-SAR images acquired simultaneously at L-, C-, and X-band over the Gulf of Mexico on 18 April 1994 at 08:11 UTC showing the strong dependence of the radar signature on radar frequency and polarization. Reproduced from Melsheimer (1998).

Fig. 6. (a), (b) Section of a Sentinel-1A SAR image acquired on 9 June 2015 at 21:53:41 UTC over the South China Sea, west of the Philippine island of Luzon, showing the radar signatures of a rain cell at VH (a) and VV (b) polarizations; (c), (d) NRCS scans along the two transects inserted in the images.

Fig.7. (a), (b) Another section of the Sentinel-1A SAR acquired on 9 June 2015 at 21:53:41 UTC showing the radar signatures of two rain cells at VH (a) and VV (b) polarizations; (c), (d) NRCS scans along two transects inserted in the images.

Fig. 8. C-band Radarsat-2 SAR image acquired in the quad-polarization mode on 15 July 2010 at 23:27 UTC off the coast of Florida (near Fort Lauderdale) showing the radar signature of a rain cell. (a) VV polarization image. (b) Next Generation Weather Radar (NEXRAD) Level III Precipitation Product (One-Hour Precipitation) on 15 July 2010 at 23:27 UTC. The rain rates varied in the rain cell between 1 and 7 mm h-1. (c) VH polarization image. (d) Variation of the NRCS at HH (blue), VV (black), HV (red), and VH (green) polarizations along the transect inserted in the images.

Fig. **9**. Maps of (a) entropy and (b) mean scattering angle of the area around the rain cells visible on the Radarsat-2 image depicted in Fig. 8.

Fig. 10. (a) Envisat ASAR image acquired in the Alternating Polarization (AP) Mode at HH polarizations during a descending satellite path over the Taiwan Strait west of Taiwan on 20 April 2009 at 01:55 UTC showing radar signatures of rain. Inserted is the look direction of the SAR antenna (thick white arrow) and the transect along which the variations of the NRCS at HH and HV polarizations has been determined, see Fig. 11. (b) Weather radar image acquired on 20 April 2009 at 02:00 UTC (10:00 LT). The rain rate was 12-24 mm h^{-1} as and the ambient wind was 5 m s^{-1} from SE.

Fig. 11. Variation of the NRCS at HH and HV polarizations along the transect inserted into the Envisat dual polarization ASAR image depicted in Fig. 10(a).

Fig. 12. (a) Envisat ASAR image acquired in the Image Mode (100 km swath width) at VV polarization over the Pearl River delta on 16 June 2008 at 14:22 UTC showing the radar signature of a large rain area located in the Pearl River delta (inside the white ellipse) as a bright area. The white arrow denotes the look direction of the SAR antenna. (b) Weather radar image of the Hong Kong Observatory acquired on 16 June 2008 at 14:18 UTC (22:18 LT). The rain rate in the circled region varied between 10 and 50 mm h^{-1} and the ambient wind was 2-4 m s^{-1} from SE.

Fig. 13. (a) Envisat ASAR VV polarization image acquired in the Image Mode over the South China Sea off the coast of Hong Kong on 6 August 2008 at 14:18 UTC showing radar signatures of a squall line. (b) Weather radar image of the Hong Kong Observatory acquired on 6 August 2008 at 14:18 UTC (22:18 LT). Here the squall line appears in the SAR image as an area of predominantly reduced NRCS (dark grey tone in the image). The rain rate in the squall line varied between 30 and 75 mm h^{-1} (heavy rain) and the ambient wind was 12-14 m s^{-1} from SE.

Fig. 14. (a) Envisat ASAR image acquired in the Wide Swath Mode (405 km swath width) at VV polarization over the southern North Sea on 9 December 2011 at 21:18 UTC showing the radar signature of a broad rain area. The white arrow denotes the look direction of the SAR antenna. (b) Weather radar image of the German Weather Service acquired on 9 December 2011 at 21:15 UTC (22:15 LT). The rain rate in the area marked by a white rhombus varied between 1 and 5 mm h^{-1} and the ambient wind was 12-14 m s^{-1} from NW.

Fig.**15**. (a) Wind field given by the NCEP model, valid for 9 December 2011 at 21:00 UTC; (b) Wind field retrieved from the Envisat ASAR image depicted in Fig. 14(a) by using the wind direction from the NCEP model valid for 9 December 2011at 21:00 UTC.

Fig. 16. Envisat SAR images acquired in the Wide Swath Mode (WSM) at VV polarizations during a descending satellite path over the South China Sea south of Hong Kong on 18 August 2011 at 02:27 UTC showing the radar signature of a rain band. Inserted is in the image the look direction of the SAR antenna (thick white arrow) and the location of Hong Kong (HK). The rain rate in the rain band was up to 50 mm h^{-1} and the ambient wind was 2-4 ms^{-1} from E.

Fig. 17. (a) Weather radar image acquired on 18 August 2011 at 02:24 UTC (10:24 LT). (b) Vertical profile of the radar reflectivity along the transect inserted in the weather radar image (a).

Fig. 18. Mean NRCS (σ^o) retrieved from ASCAT data (VV polarization) as a function of wind speed for different rain rates. (a) NRCS measured by ASCAT at the Wind Vector Cell (WVC) number 11 by the fore-beam at an incidence angle of 52.8^o; (b) Same, but measured by the mid-beam at an incidence of 41.7^o. Reproduced from Lin et al. (2013).

Fig. A1. Scattering mechanism as identified in the H/α plane. Reproduced from Pottier (2007).